

CONCEPTUAL DESIGN AND HEAT TRANSFER INVESTIGATION OF A
DENSE GRANULAR FLOW SOLAR RECEIVER

A THESIS SUBMITTED TO
THE GRADUATE SCHOOL OF NATURAL AND APPLIED SCIENCES
OF
MIDDLE EAST TECHNICAL UNIVERSITY

BY

EVAN FAIR JOHNSON

IN PARTIAL FULFILLMENT OF THE REQUIREMENTS
FOR
THE DEGREE OF MASTER OF SCIENCE
IN
MECHANICAL ENGINEERING

FEBRUARY 2017

Approval of the Thesis:

**CONCEPTUAL DESIGN AND HEAT TRANSFER INVESTIGATION OF A
DENSE GRANULAR FLOW SOLAR RECEIVER**

submitted by **Evan Johnson** in partial fulfillment of the requirements for the degree
of **Master of Science in Mechanical Engineering Department, Middle East
Technical University** by,

Prof. Dr. M. Gülbin Dural Ünver
Dean, Graduate School of **Natural and Applied Sciences**

Prof. Dr. Raif Tuna Balkan
Head of Department, **Mechanical Engineering**

Prof. Dr. Derek K. Baker
Supervisor, **Mechanical Engineering Dept., METU**

Assoc. Prof. Dr. İlker Tari
Co-Supervisor, **Mechanical Engineering Dept., METU**

Examining Committee Members:

Ass't Prof. Dr. Özgür Bayer
Mechanical Engineering Dept., METU

Prof. Dr. Derek K. Baker
Mechanical Engineering Dept., METU

Assoc. Prof. Dr. İlker Tari
Mechanical Engineering Dept., METU

Assoc. Prof. Dr. Serkan Kıncal
Chemical Engineering Dept., METU

Prof. Dr. Aynur Eray
Physics Department, Hacettepe University

February 3, 2017

I hereby declare that all information in this document has been obtained and presented in accordance with academic rules and ethical conduct. I also declare that, as required by these rules and conduct, I have fully cited and referenced all material and results that are not original to this work.

Name, Last name :

Signature :

ABSTRACT

CONCEPTUAL DESIGN AND HEAT TRANSFER INVESTIGATION OF A DENSE GRANULAR FLOW SOLAR RECEIVER

Johnson, Evan Fair
Supervisor: Prof. Dr. Derek Baker
Co-Supervisor: Assoc. Prof. Dr. İlker Tari

January 2017, 77 pages

Solid particles have previously been proposed as an alternative to molten salt as a heat transfer and heat storage medium for concentrating solar power plants. While previous solid particle solar receiver designs use fluidized or falling particles, the new type of receiver proposed in this thesis uses a gravity-driven flow of particles in a dense granular flow regime. Through experimentation with sand, the flow and heat transfer properties were studied in two geometries: vertical tubular and vertical parallel plate. The effective thermal conductivity of the flowing sand, calculated from experimental results, was used to model a 5 by 5 meter square, finned solar receiver in ANSYS Fluent. Four different fin configurations were modeled with two levels of uniform radiative flux. One fin configuration was studied using a concentric radiative flux distribution with a peak of 600 kW m^{-2} , and results show an overall thermal efficiency of 66.5% and a maximum temperature of 1047°C reached on the absorber surface.

Keywords: dense granular flow, solid particle, solar receiver

ÖZ

YOĞUN TANECİKLİ AKIŞ GÜNEŞ ALICISININ KURAMSAL TASARIMI VE ISI AKTARIMI İNCELEMESİ

Johnson, Evan Fair
Danışman: Prof. Dr. Derek Baker
Eş-danışman: Doç. Dr. İlker Tarı

Ocak 2017, 77 sayfa

Katı tanecikler eriyik tuzlara alternatif olarak daha önce güneş enerji santrallerinde ısı aktarımı ve ısı saklama ortamı olarak önerilmiştir. Daha önceki katı parçacıklı güneş alıcısı tasarımları akışkanlaştırılmış veya düşen parçacıkları kullanırken, bu tezde önerilen yeni tip alıcı yoğun tanecikli akış rejimindeki parçacıkların yerçekimi ile akışını kullanmaktadır. Kum kullanılan deneylerle, dikey tüp ve dikey paralel plaka geometrilerinde akış ve ısı aktarımı özellikleri çalışıldı. Deneylerden akan kumun etkin iletkenliği elde edildi ve bu sonar 5 metreye 5 metre boyutlu kanatçıklı güneş alıcısının ANSYS Fluent modelinde kullanıldı. Dört ayrı kanatçık geometrisi modellendi, ve iki ayrı homojen ışınma akısı göz önüne alındı. Bir kanatçık konfigürasyonu 600 kW m^{-2} üst değerli konsentrik ışınma akısı dağılımı için çalışıldı ve sonucunda %66.5 ısı verim ve emici yüzeyde 1047°C maksimum yüzey sıcaklığına ulaşıldı.

Anahtar Kelimeler: yoğun tanecikli akış, katı tanecikler, güneş alıcısı

ACKNOWLEDGEMENTS

Many people deserve thanks for helping in this work, most notably Dr. Derek Baker and Dr. İlker Tarı for their guidance, ideas, thoughtful feedback, and encouragement. Mustafa Yalçın was instrumental in the construction of the laboratory setup, Serdar Hiçdurmaz offered endless help both in modeling and interpreting Turkish language and culture, and special thanks go to Mohammad Rezaeimoghaddam for helpful ideas and advice.

TABLE OF CONTENTS

ABSTRACT.....	v
ÖZ	vi
ACKNOWLEDGEMENTS.....	vii
TABLE OF CONTENTS.....	viii
LIST OF TABLES.....	xi
LIST OF FIGURES	xii

CHAPTERS

1. INTRODUCTION TO SOLID PARTICLE SOLAR RECEIVERS.....	1
1.1 Direct Falling Particle Receivers	3
1.2 Indirect Falling Particle Receivers.....	4
1.3 Particle Suspension Receivers	5
1.4 Centrifugal Receivers.....	5
2. PROPOSAL OF A NOVEL RECEIVER AND MODELING METHODS.....	7
2.1 Objectives and Scope.....	7
2.2 Proposal of a Novel Receiver Category: Dense Granular Flow	8
2.3 Modeling Methods Considered.....	10
2.4 Modeling Particle Mixtures	11
3. MATERIAL PROPERTIES	15
3.1 Particle Diameter.....	15
3.2 Density and Volume Fraction	17
3.3 Specific Heat	17
4. EXPERIMENTS: VERTICAL TUBE.....	19
4.1 Flow Rate Experiments.....	19
4.2 Plug Flow Approximation.....	21
4.3 Heat Transfer Experiments	22

4.4 Summary of Tube Experiments	27
5. EXPERIMENTS: PARALLEL PLATES	29
5.1 General Experimental Setup	29
5.2 Flow Regulation and Measurement	31
5.3 Heater Surface Thermocouple Attachment Method	32
5.4 Thermocouple Placement	33
5.5 Steps to Minimize Undesired Heat Flow	34
5.6 Sand Outlet Temperature Measurements.....	35
5.7 Sample Results.....	37
5.8 Analysis of Experimental Results.....	39
5.9 Calculation of k_{eff} in the Fully Developed Region	41
5.10 Calculation of k_{eff} in the Entrance Region	43
5.11 Results and Discussion on k_{eff}	45
6. MODELING OF THE RECEIVER	47
6.1 Overview.....	47
6.2 Governing Equations	49
6.3 Boundary Conditions	50
6.4 Mesh Independence Study	52
6.5.1 Receiver Modeling with Uniform Radiative Flux	54
6.5.2 Results and Discussion for Uniform Radiative Flux	55
6.6.1 Receiver Modeling with Concentric Radiative Flux	59
6.6.2 Results and Discussion for Concentric Radiant Flux	60

7. CONCLUSIONS.....	65
8. FUTURE WORK.....	67
REFERENCES	69
APPENDICES	
A: UDF FOR MODELING HEAT TRANSFER TO ABSORBER SURFACE	73
B: NUSSELT NUMBER DERIVATION FOR PLUG FLOW THROUGH INFINITE PARALLEL PLATES	75

LIST OF TABLES

TABLES

Table 2.1. Comparison of properties of fluids to two-phase mixtures in dense granular flow.	12
Table 3.1. Sauter Mean Diameters of sand samples.....	17
Table 3.2. Density and volume fraction of the four sand types tested.	17
Table 5.1. Bulk outlet temperature measured with three different methods.	36
Table 5.2. k_{eff} values calculated by matching experimental data to Fluent modeled results.....	45
Table 6.1. Parameters used for modeling receiver.	52
Table 6.2. Mesh size effect on outlet temperature.....	53
Table 6.3. Verification of conservation of energy.....	53
Table 6.4. Heat gains and loss from a 5x5 meter receiver, with four fin configurations and two uniform radiative flux values studied.	56
Table 6.5. Absorber temperatures and thermal efficiency for the eight cases.	56
Table 6.6. Heat loss and gain for left half of receiver with a concentric radiative flux, divided into ten sections.	62

LIST OF FIGURES

FIGURES

Figure 1.1. Depiction of the main components of a solid particle CSP plant.....	2
Figure 1.2. Falling Particle Receiver (a) and a single riser tube of a Particle Suspension Receiver (b).	4
Figure 2.1. Single tube studied at lab scale (a), and full receiver made from multiple tubes (b).	8
Figure 2.2. Finned annular receiver.	9
Figure 2.3. Three views of a receiver with enhanced light trapping properties, with sand flowing downward through fins.	9
Figure 3.1. Sand samples from left to right: Fine, Medium, Coarse, Sand #4.....	15
Figure 3.2. Mass percentage of particles in sieves, for (a) Fine, (b) Medium, and (c) Coarse sand types.....	16
Figure 3.3. Measured specific heat values of sand at varying temperatures.....	18
Figure 4.1. Laboratory setup (left), packed flow regime (middle), and free fall flow regime (right).	20
Figure 4.2. Maximum mass flux for three tube sizes and three sand grain sizes, plotted with respect to (a) diameter and (b) cross-sectional area.....	20
Figure 4.3. Image of video footage used to calculate particle velocity at the wall... ..	22
Figure 4.4. Heated copper tube with 8 heating elements.	24
Figure 4.5. Steady state tube surface temperatures (lines) and sand inlet and outlet temperatures (icons) with four 4.75 mm orifice holes (a), one 9.4 mm orifice (b), one 11.0 mm orifice (c), and one 12.4 mm orifice (d).....	25
Figure 4.6. Heat transfer coefficient at various mass flux values.	27
Figure 5.1. Side view of channel construction (a), front view (b), and cross section (c).	30
Figure 5.2. Heated channel with ceramic insulation.	31
Figure 5.3. Restriction plate (left) and sand flowing from channel (right).....	32

Figure 5.4. Thermocouples measuring heated surface temperature, secured under the head of a brass screw. Fiberglass insulating sleeve in white.....	32
Figure 5.5. Resistance heater wire wrapped around glass material, with steel backing plate removed. Thermocouple wires pass through heater and out front face.	33
Figure 5.6. Thermocouple placement on heated copper surface, dimensions in mm.	34
Figure 5.7. Insulating nozzle to mix and concentrate flow.	35
Figure 5.8. Insulated container with thermocouple for measuring bulk temperature of particles.....	36
Figure 5.9. Transient response of heated surface temperatures.....	38
Figure 5.10. Sample data showing heated surface temperatures and bulk inlet and outlet temperatures.	38
Figure 5.11. Heated and insulated surface temperatures parallel plate flow reaching a fully developed region state.....	39
Figure 5.12. Uniform heat flux boundary condition applied directly to sand (a), and uniform heat flux applied to a copper plate which contacts sand (b).	41
Figure 5.13. Heated surface temperatures, showing experimental and modeled results with various thermal conductivity values.	44
Figure 6.1. Heat flows to and from receiver (left), and corner of the finned receiver (right).	47
Figure 6.2. Fin cross section showing symmetry lines (a) and single fin used for CFD modeling (b).....	48
Figure 6.3. Cross section view of fin (gray) and sand (blue) with Mesh 1 (top) and Mesh 2 (bottom).	52
Figure 6.4. Cross sections of 5 meter long fins modeled with uniform radiant heat flux assumption, dimensions in millimeters.	54
Figure 6.5. (a) Fin configuration C shown in 3D, and (b) fin modeled in Fluent after reducing the problem with planes of symmetry.	55
Figure 6.6. Heat gains and losses as a percentage of incident radiation.	57
Figure 6.7. Temperature distribution in sand at outlet for configurations C (left) and D (right), with a uniform 600 W m^{-2} radiant flux.....	58
Figure 6.8. Concentric flux distribution on 5 m square receiver.....	59
Figure 6.9. Heat gain and losses from various sections of the receiver.	62

Figure 6.10. Maximum and average temperature of the absorber surface for ten fins modeled..... 63

CHAPTER 1

INTRODUCTION TO SOLID PARTICLE SOLAR RECEIVERS

Concentrating Solar Power (CSP), also known as Solar Thermal Electricity, for electricity production has been gaining attention and investment in recent years. It has one main advantage over photovoltaic and other renewable energy technologies; energy is collected in the form of heat, which can be stored in large quantities of heated material until it is needed for electricity production. Thus, unlike other renewable energy sources, CSP can provide a predictable and reliable electricity output, generating power at night or when electricity demand peaks. With this advantage in mind, research is being conducted at institutions worldwide to improve the thermal efficiency and reduce both the Levelized Cost of Energy and capital cost of these power plants.

Central Receiver type CSP plants use a large field of individually controlled mirrors, called heliostats, to concentrate solar radiation at the top of a tower, as depicted in Figure 1.1. CSP plants often use molten salt as a heat transfer fluid; it is pumped to the top of the tower where it heats up inside the solar receiver before returning to ground level for use. Molten salt is also often used for sensible heat storage by keeping a large quantity in an insulated tank for later use. However, molten salt has several drawbacks, which is why a growing number of researchers have proposed using solid particles (as opposed to a fluid) to fulfill the roles of the heat transfer medium and the heat storage medium. There are several reasons why solid particles have the potential to outperform molten salt and other liquid materials:

- 1) Molten salts chemically break down above 600°C , which imposes a limit of 600°C on the power cycle, typically a steam Rankine cycle. Several candidate solid particles can withstand temperatures in excess of 1000°C , which would enable higher Carnot and actual thermal efficiencies of the power plant [1].

- 2) Temperatures nearing 1000°C may enable other power cycles, such as air Brayton or supercritical carbon dioxide cycles, which are currently not feasible with the 600°C limit. This would increase efficiency substantially [1].
- 3) Molten salts freeze around 220°C . Electrical heating and control systems are needed to maintain the salt in a liquid state, which is a source of cost and operational complexity. In solid particle based power plants, these temperature regulation systems would not be necessary as particles remain in the solid physical state over a wide range of temperatures [1].
- 4) A very large quantity of storage material is needed to run a large power plant for several hours, so cost per energy stored is an important metric. Compared to molten salts, some solid particles, such as sand, are very inexpensive.

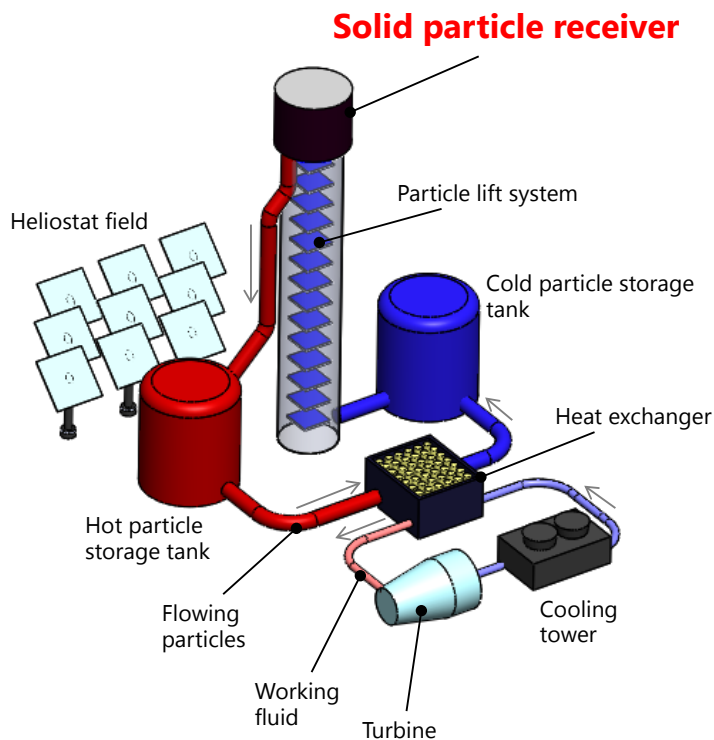


Figure 1.1. Depiction of the main components of a solid particle CSP plant.

Candidate materials that have been studied are sand, bauxite, and ceramics such as silicon carbide [2][3]. The National Renewable Energy Lab (NREL) estimated the capital cost of a sand-based thermal energy storage system to be 75% less than a

traditional molten salt system. Overall power plant cost could decrease by 20% assuming the same Rankine cycle, and it would drop further if employing an advanced power cycle such as air Brayton [1]. With these economic and operational benefits, solid particle systems are attracting the attention of researchers and institutions worldwide.

This thesis focuses on the solar receiver, the part at the top of the tower which absorbs concentrated radiation and delivers it to the heat transfer medium. In this thesis, a new type of solid particle receiver is proposed, studied experimentally at lab scale, and modeled at a larger scale with computational fluid dynamics (CFD) in ANSYS Fluent. This thesis focuses on sand as the solid particle of choice because of its very low cost and abundance in the arid regions where CSP plants are well suited. The currently studied solid particle receivers generally fall into the following categories, and the benefits and challenges of each design are listed below.

1.1 Direct Falling Particle Receivers

Particles are dropped from the top of the receiver, and they are *directly* irradiated through an open window as they fall, as shown in Figure 1.2 (a). This is the most widely studied design, with early work performed at Sandia National Laboratory as early as 1988 [4]. More recent research at Sandia features a 1 MW demonstration receiver [3].

Benefits: Particles are directly irradiated, so a very high heat flux is possible. Any receiver with an intermediate absorber surface may be limited by the radiative flux it can withstand, with excessive flux leading to the absorber melting. It is also a mechanically simple design.

Drawbacks: Ideally, the residence time of particles in a receiver could be adjustable in order to maintain a constant output temperature even in varying environmental conditions. As particles are falling, this affords little or no control over the speed or residence time of the particles, and the receiver cannot be adjusted to maintain a constant output temperature. Particles on the edges of the receiver also gain less heat than those in the center due to the typical peak in radiation at the center. To combat

these issues, researchers have proposed recirculating particles for multiple passes or putting obstructing materials in place to slow the fall of particles [3]. Furthermore, prototypes have shown difficulty maintaining proper flow in windy conditions, and particles are often lost out the window [5]. Additionally, particles must have a high absorptivity as they are absorbing radiation, so studies focus on highly absorptive particles such as bauxite, as opposed to the more economical option of sand [2].

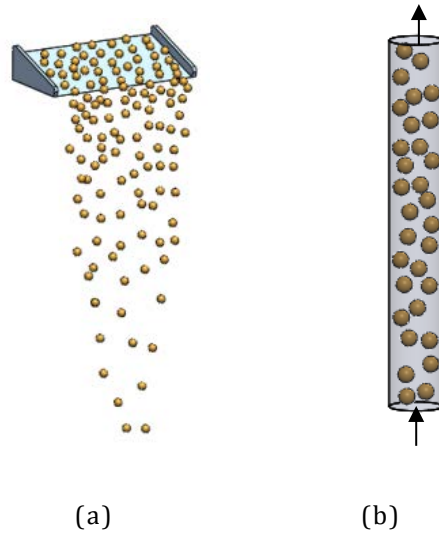


Figure 1.2. Falling Particle Receiver (a) and a single riser tube of a Particle Suspension Receiver (b).

1.2 Indirect Falling Particle Receivers

Particles fall behind an opaque absorber surface, which absorbs the concentrated radiation and then transfers heat to the particles.

Benefits: Disruptions of particle flow and loss due to wind are eliminated. High radiation trapping designs are possible through various absorber geometries [6].

Drawbacks: Similar to Direct Falling Particle Receivers, there is little control over particle residence time. As with any receiver which has an absorber surface, the maximum heat flux would be lower than that of a Direct Falling Particle Receiver [5].

1.3 Particle Suspension Receivers

Similar to a fluidized bed, particles are lifted into suspension by air jetted in at the bottom of a riser tube (Figure 1.2 (b)). Air carries the particles upward, maintaining the particle flow rate and a solid volume fraction of up to 30-40% [7].

Benefits: Air jet speed gives some flow rate control. High heat transfer coefficients, up to $1116 \text{ W m}^{-2} \text{ K}^{-1}$, have been found experimentally due to the high velocity of the air-sand mixture [8].

Drawbacks: Due to fluidization constraints, the mass flow rate through a certain tube size (often expressed as a mass flux) is limited. Researchers have considered mass flux limits of 40 and $45.1 \text{ kg m}^{-2} \text{ s}^{-1}$ [9][8] which may inhibit the scalability to larger systems. Additionally, a meaningful amount of electric power is needed for the air jets, and the heated air, which must be vented, represents a heat loss as well [9]. Lastly, most studies investigate fluidization using small particles such as ceramic powders [7]. Larger particles, such as sand grains, are more difficult to fluidize.

1.4 Centrifugal Receivers

Particles are fed into a rotating drum and forced to the wall of the drum due to the rotational forces. Concentrated sunlight enters the bottom of the drum, which is open, and light strikes particles directly [10][11].

Benefits: Drum rotation speed gives control over the downward flow rate of particles. Particles are directly irradiated, so a high heat flux can be used.

Drawbacks: Reliability of a rotating drum at elevated temperatures may be a problem in actual deployments, and the geometry of a circular drum does not readily scale to large receivers capable of absorbing several hundred MW_{th} [5].

CHAPTER 2

PROPOSAL OF A NOVEL RECEIVER AND MODELING METHODS

2.1 Objectives and Scope

Previous solid particle receivers have used falling or fluidized particles, but no previous work studies a receiver working in the dense granular flow regime, where particles descend with gravity in a fully-packed manner through the receiver. This constitutes a fifth category of receiver, featuring completely different flow and heat transfer mechanisms than the others.

While the dense granular flow (DGF) receiver concept was developed completely independently, a recent conference paper has also now proposed using the DGF regime, which was published after the literature survey and initial experiments for this thesis had already been conducted. However, only small-scale lab tests and modeling were performed on tubes [12][13]. No mention of the operation or benefits of such a receiver were given, and no full-scale receiver design has previously been modeled or even proposed.

The objectives of this thesis are to:

1. Conceptually analyze the benefits and drawbacks of the DGF receiver category and compare it to previously studied designs
2. Define a method to model large-scale DGF receiver designs
3. Model a large-scale DGF receiver to determine
 - a. Thermal efficiency
 - b. The maximum temperature reached on the receiver to verify the receiver will not melt

With an entirely new receiver category proposed, many different designs could be studied and optimized. To limit the scope of this thesis, only flat, finned receiver type was investigated. Four different fin configurations and several levels of radiative flux were studied. With the modeling method established in this thesis,

various receiver designs can be studied in the future by altering variables such as the receiver geometry, particles, and materials.

2.2 Proposal of a Novel Receiver Category: Dense Granular Flow

Starting with the desired criteria of easy flow control, high mass flux, minimal parasitic power, and the ability to use sand as the particle, an alternative receiver design can be envisioned where particles flow downward through a vertical absorber tube in a fully-packed manner, similar to a fluid draining from a funnel through a vertical pipe. Here, unlike Falling Particle Receivers, particles would *not* be in free fall; the downward flow rate of particles would be regulated by a valve at the outlet. This fully-packed flow regime is referred to as the dense granular flow regime [14]. In Figure 1.1 Figure 2.1 (a) a single absorber tube is shown for simplicity and studied at lab scale. A DGF receiver could be designed with many different geometries, including multiple absorber tubes as in Figure 2.1 (b), a vertically oriented annulus with fins (Figure 2.2), or an enhanced light trapping design (Figure 2.3).

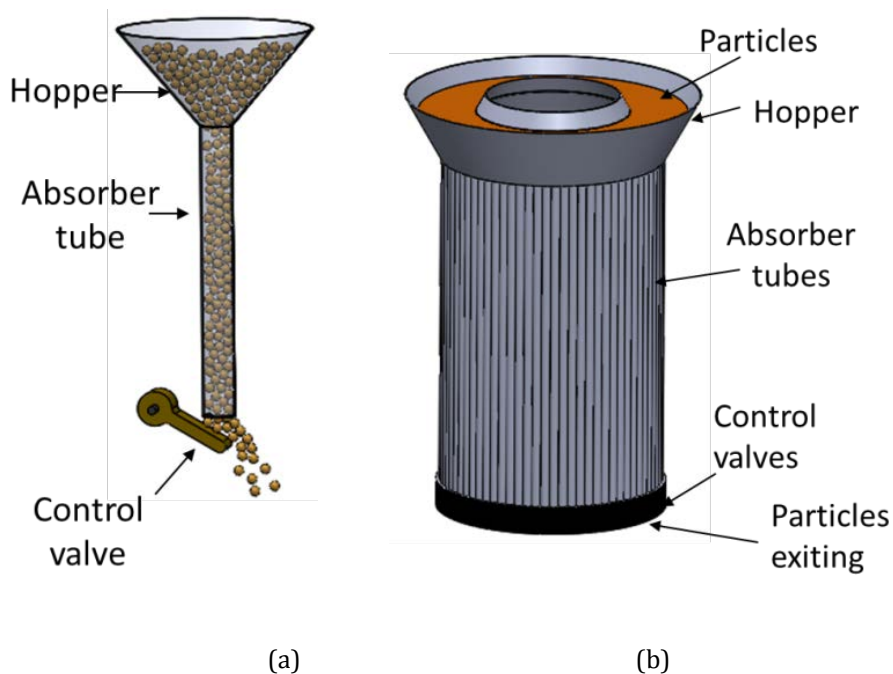


Figure 2.1. Single tube studied at lab scale (a), and full receiver made from multiple tubes (b).

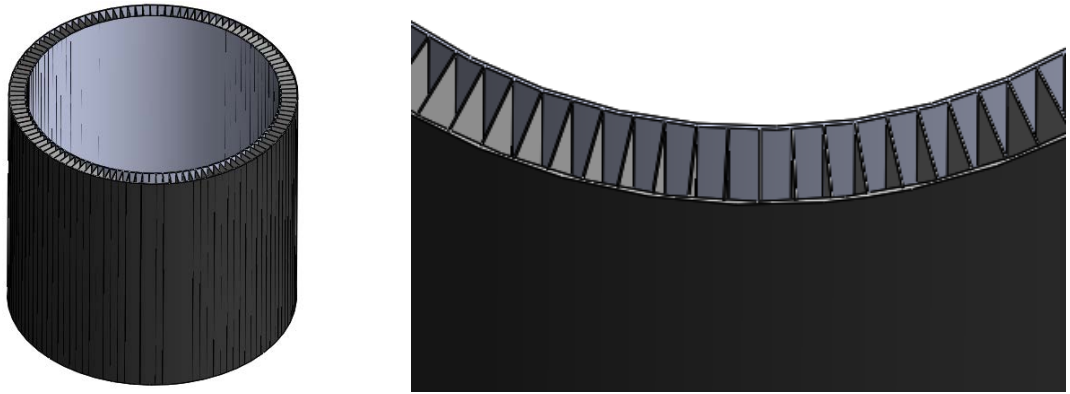


Figure 2.2. Finned annular receiver.

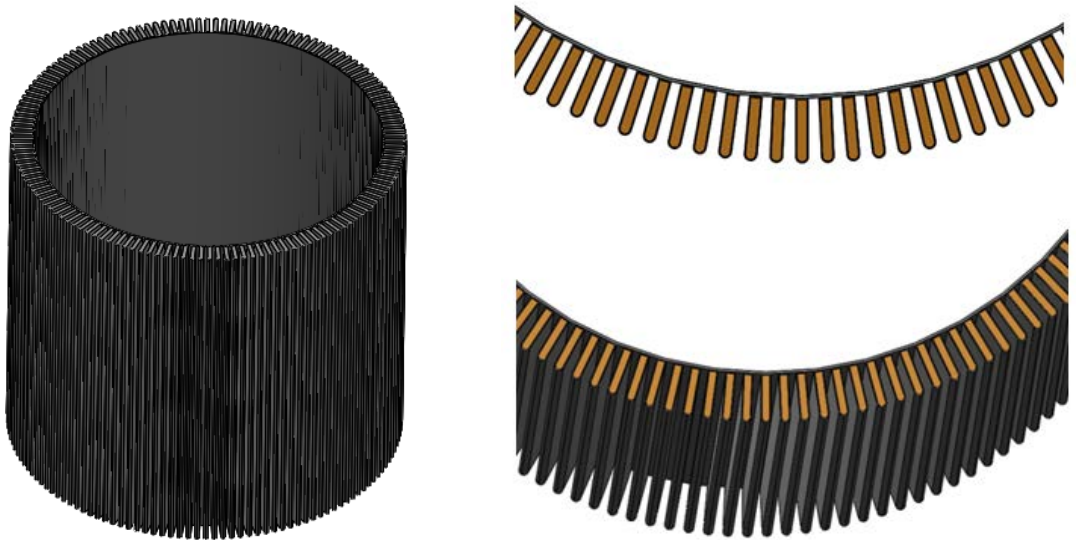


Figure 2.3. Three views of a receiver with enhanced light trapping properties, with sand flowing downward through fins.

Anticipated Benefits

- 1) Flow rate would be easily and fully controllable with a valve, from stationary up to the maximum mass flux allowable. Residence time and particle output temperature could be readily controlled.
- 2) Flow would be dense, so a higher mass flux is expected to be possible relative to fluidized systems.

- 3) Cost, parasitic power input, and mechanical complexity would be minimized by eliminating air jetting, rotating drum systems, or recirculation systems.
- 4) Without fluidization or emissivity requirements of the particle, sand or other inexpensive particles could be used.
- 5) No particles would be lost through an aperture as in Direct Falling Particle Receivers.
- 6) Low receiver erosion would be expected due to reduced particle speeds and low pressure.

Potential Drawbacks

Particles in the dense granular flow regime have low velocity and mixing, so the heat transfer coefficient from receiver to sand is expected to be low compared to fluidized flow regimes. Achieving a high thermal efficiency given the anticipated low heat transfer coefficient is a challenge and the focus of this research.

2.3 Modeling Methods Considered

Two methods were considered to model the proposed receiver:

- 1) **Discrete Element Method.** To model the receiver computationally, the Discrete Element Method (DEM) is generally used for dense granular flows [15]. This is an active area of research, and complex to solve even for simple particle flows [14]. To solve the equations of motion, every collision between particles is modeled, making the number of calculations extremely high when modeling small particles such as sand grains. In a dense granular flow, the contact interactions between particles govern the flow, and fluid interactions are generally negligible [14]. However, for problems with heat transfer, conduction and convection through the interstitial fluid plays a large role and must be considered along with radiative and particle-particle conduction effects. Solving these equations for both flow and heat transfer is extremely computationally intense when particle diameters are small, and

modeling a 3D receiver in the size range of 5 by 5 meters would take an enormous amount of computing power.

- 2) **Semi-Empirical Method.** In this method, experiments are run to classify the flow and heat transfer characteristics of the bulk mixture under conditions similar to the final application. Results from experiments are then used as inputs to the CFD model of a single-phase fluid.

Compared with DEM, the semi-empirical method dramatically reduces the computational time required, which enables modeling of the large domain needed for a solar receiver. Furthermore, performing experiments has the valuable benefit of revealing any unexpected problems which will eventually appear in an actual receiver but would not be discovered through purely computational modeling.

The semi-empirical method was performed with the following sequence of steps:

- 1) Determine material properties of particles. (Chapter 2)
- 2) Study heat transfer and flow in a vertical tube to understand the fundamentals of dense granular flow and uncover any basic problems with a DGF receiver. (Chapter 3)
- 3) Experimentally study heat transfer in vertical, parallel plate flow, with heat flux applied to one side. (Chapter 4)
- 4) Find “effective thermal conductivity” (k_{eff}) of sand and air mixture. (Chapter 4)
- 5) Use k_{eff} of sand mixture to perform CFD modeling of a finned, 5 meter square, flat receiver. Outputs include thermal efficiency and maximum temperature on receiver. (Chapter 5)

2.4 Modeling Particle Mixtures

In the dense granular glow regime, the flow of particles is near the packing limit, and motion is governed by particle-particle contacts; the interstitial fluid (air in this case) has little to no effect on the flow of the particles [16]. The fluid does, however, play an important role in the heat transfer, as air conducts and convects heat in the spaces between the particles. The actual heat transfer, fluid mechanics, and solid

mechanics involved in two-phase flows, are quite complex, but the properties of the overall mixture can be compared to single-phase fluids by using “bulk” or “effective” properties. Table 2.1 highlights several of the main differences between the properties of fluids and those of mixtures.

Table 2.1. Comparison of properties of fluids to two-phase mixtures in dense granular flow.

Parameter	Fluid	Dense Granular Flow
Heat transfer coefficient (h)	For internal, fully-developed, laminar flow, Nusselt number and h are constant, <i>not</i> a function of flow rate [17].	Heat transfer dependent upon particle-particle, particle-gas, and particle-wall interactions. Previous experiments [18] show h is a function of flow rate.
Thermal conductivity (k)	k is a material property, independent of flow characteristics.	“Effective” or “bulk” conductivity of packed particles depends upon various factors, including: <ul style="list-style-type: none"> • Solid material properties • Fluid material properties • Particle size • Particle shape • Packing fraction • “Granular temperature”
Wall shear condition	No-slip condition applies to particles.	Almost full-slip of particles [18] [19].

One of the central differences is that for an internal, fully developed laminar flow, the heat transfer coefficient does not vary with flow rate, whereas with a granular flow, the heat transfer coefficient is a function of flow. According to [18] and [19], this is because in flowing mixtures, the conductivity of the bulk material is a function of the actual or “molecular” conductivity of the solid and fluid phases, plus the added heat transfer due to particles moving and mixing as they flow. Factoring in many variables including flow rate, the thermal conductivity of a mixture can be calculated to describe the “effective” or “bulk” conductivity (k_{eff}). Unlike the thermal conductivity of a single phase, k_{eff} is not a universal material property, but if it is known for a particular flow, it can be useful for modeling.

In [19], equations have been developed to find k_{eff} , which is a function of material properties as well as the “granular temperature”. Granular temperature is not

actually a temperature, but it is analogous to how temperature describes the velocity fluctuations of molecules; in mixtures, granular temperature is a measure of velocity fluctuations of particles. While the relationship of granular temperature to k_{eff} provides some background and qualitative explanation, granular temperature is unfortunately not an easy parameter to measure with laboratory equipment, so it does not provide a simple means of finding k_{eff} . Therefore, k_{eff} will be found by drawing comparisons to single phase fluid flow in Sections 5.9 and 5.10.

Natarajan et al. [18] studied heat transfer to glass particles through vertical parallel plates and compared their findings with several previous studies. Their experiments showed the heat transfer coefficient increases significantly with flow rate until a peak is reached around 12 cm s^{-1} and then falls off slightly at higher flow rates. They attributed this peak to two opposing factors. Increasing the flow rate increases the particle motion and therefore heat transport, but at higher velocities the bulk density near the wall decreases, leaving a low-conductivity air gap and reducing heat transfer. The second important conclusion drawn by Natarajan et al. is that inclined chutes heated on the bottom side (as opposed to vertical chutes) have higher heat transfer, and their peak heat transfer occurs at much higher velocities. This is attributed to gravity forcing particles to the wall and reducing the air gap between wall and particles.

Experimental studies have focused on flows where the heated section is short and the cross sectional flowing area is large, so flow did not become thermally fully developed [20][18]. Heat transfer coefficients have been calculated as for external flows with Equation (2.1), where T_{inf} is taken as the entering bulk temperature.

$$h = \frac{Q}{A(T_{surface} - T_{inf})} \quad (2.1)$$

The geometry of a solar receiver will be long, at least 5 meters, and the flowing section will be thin to maximize the contact surface area with the receiver, so the heat transfer coefficient should be found for an internal flow, where the bulk temperature at each location is taken as T_{inf} . While trends are expected to be similar, the previous experimental studies do not capture the behavior for internal flows with

a significant or fully developed boundary layer. Therefore, the results cannot be used for modeling of the proposed receiver, which is made of a long, thin section and will certainly have a substantial boundary layer. Therefore, as part of this work, experiments were designed to measure the flow characteristics, heat transfer coefficients, and k_{eff} values for sand in conditions similar to those in the proposed receiver.

CHAPTER 3

MATERIAL PROPERTIES

3.1 Particle Diameter

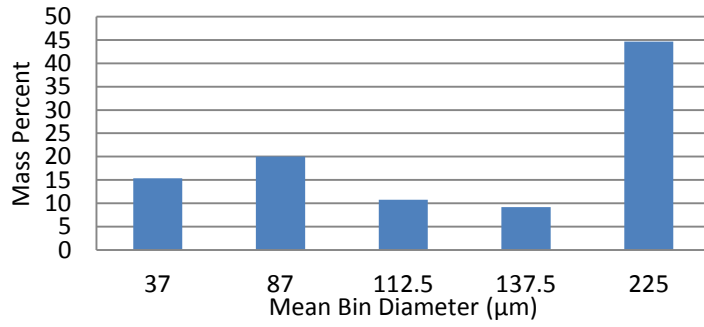
Originally, three sand samples were obtained, sourced from a sandstone quarry near Denizli, Turkey. These samples will be referred to here as Fine, Medium, and Coarse, and tubular heat transfer tests were run with these three sand types. After finishing the tubular heat transfer tests, a much greater quantity was needed for the parallel plate flow experiments, so a fourth batch of sand was purchased, referred to as Sand #4. Samples are shown in Figure 3.1 below.



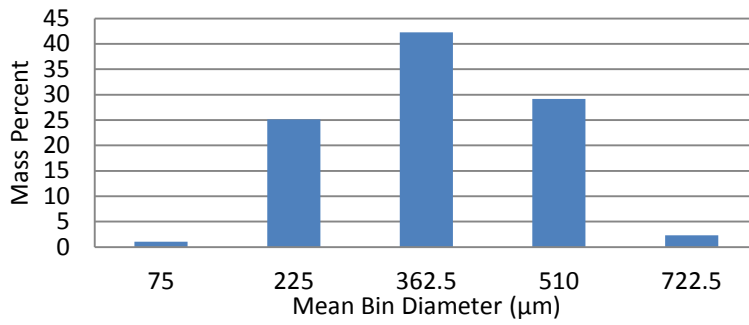
Figure 3.1. Sand samples from left to right: Fine, Medium, Coarse, Sand #4.

Using progressively smaller sieves, the particles were divided into diameter ranges, as shown in Figure 3.2. The Sauter Mean Diameter (SMD) was calculated with Equation (3.1) [21] and presented in Table 3.1. After separating into various diameter ranges, m_i is the mass of the sand in that particular range, d_{av} is the sieve size in the middle of the range, and M_{tot} is the total mass from all ranges. SMD testing was performed for the first three samples, but not for the fourth. However, a visual inspection as well as the measured bulk density indicate the grain size of Sand #4 is in between the Medium and Coarse sands.

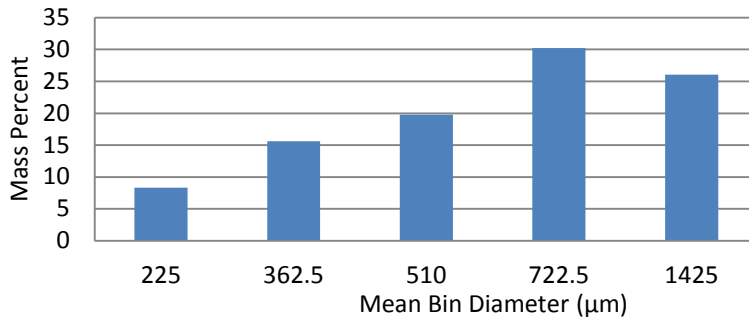
$$SMD = \sum_i (m_i * d_{av}) / M_{tot} \quad (3.1)$$



(a)



(b)



(c)

Figure 3.2. Mass percentage of particles in sieves, for (a) Fine, (b) Medium, and (c) Coarse sand types.

Table 3.1. Sauter Mean Diameters of sand samples.

Sand Sample	Sauter Mean Diameter (μm)
Fine	99
Medium	346
Coarse	559

3.2 Density and Volume Fraction

The bulk density of each sand type was found by weighing a 1000 mL sample. This was performed several times and results were averaged. The volume fraction, or the percentage of the bulk volume actually occupied by solid particles, was found by adding a known volume of water and measuring the final combined volume. Results are shown in Table 3.2 below.

Table 3.2. Density and volume fraction of the four sand types tested.

Sand Sample	Bulk Density	Volume Fraction
Fine	1368	56%
Medium	1499	57%
Coarse	1609	62%
#4	1537	-

3.3 Specific Heat

Since a wide variety of specific heat values are found in literature and properties vary by geographic location, the specific heat of sand used for experiments was tested using a Differential Scanning Calorimeter. Fine, Medium, and Course samples were tested along with three other sands collected from locations in Morocco, Abu Dhabi, and Gocek, Turkey (Figure 3.3). Unfortunately, most of the samples show very low or even negative specific heat values at room temperature, indicating a calibration error, so results were *not* used in the following calculations. However, the specific heat test is included for completeness as it shows the general trend of increasing specific heat with temperature, which will be an important relationship to incorporate in future work. Without a measured value of specific heat, a value of $776 \text{ J kg}^{-1} \text{ K}^{-1}$ was chosen as the middle of the range for dry quartz sand [22].

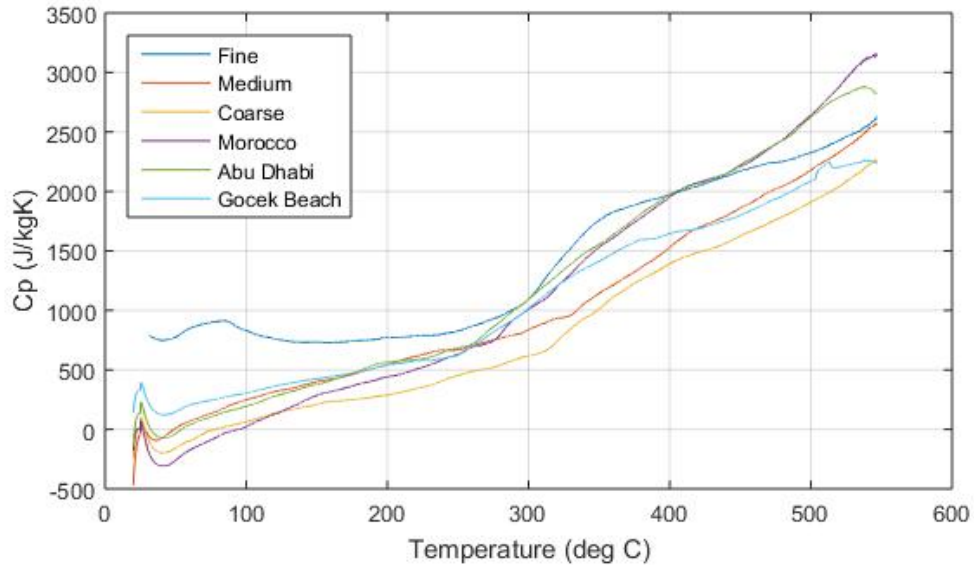


Figure 3.3. Measured specific heat values of sand at varying temperatures.

CHAPTER 4

EXPERIMENTS: VERTICAL TUBE

Initial experiments were conducted to study heat transfer and particle flow in vertical tubes. This was an important initial step, which allowed for better understanding of the characteristics and trends of sand in the DGF regime. However, the heat transfer coefficients found here were *not* used in CFD modeling of the final receiver design, as the parallel plate geometry is more applicable to the final receiver design that was chosen for modeling.

4.1 Flow Rate Experiments

Experiments were run using the laboratory setup shown in Figure 4.1. It features a large hopper to feed the vertical tube, and mass flow was measured using a scale placed below the collecting container. Unlike fluid flow, particle flow rate through an opening does *not* depend on head height of particles above due to particle friction forces [23], so a constant particle flow rate is easily maintained.

Initial non-heated tests were run with glass tubes to observe sand flow and investigate any unexpected flow regimes. The glass tubes had inner diameters of 7.75, 9.75, and 15.25 mm and a length of 1.2 m.

Initial testing showed that with an orifice plate, valve, or a restriction over the outlet, a dense sand flow was achieved, and no visible air pockets or blockages due to friction were observed. However, if the restriction or valve was removed, sand entered a different flow regime where it was in free fall through air, and the tube became no longer fully packed. As seen in Figure 4.1, the two flow regimes are easily distinguishable. Since free-fall flow is not desired, a certain maximum flow rate exists where the fully-packed flow regime can be maintained. To find the transition point between free fall and the fully-packed flow regimes, a fitting with an adjustment screw was attached to the tube outlet (Figure 4.1, middle) and adjusted until the flow was just under the transition point. This maximum flow rate,

expressed as a mass flux, was determined for each sand and tube size, and the results are plotted in Figure 4.2.

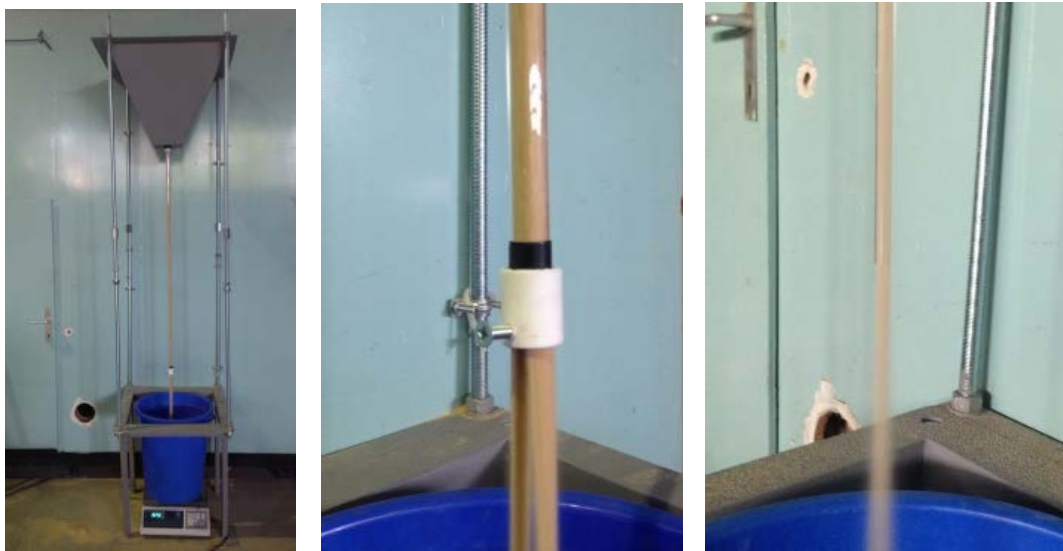


Figure 4.1. Laboratory setup (left), packed flow regime (middle), and free fall flow regime (right).

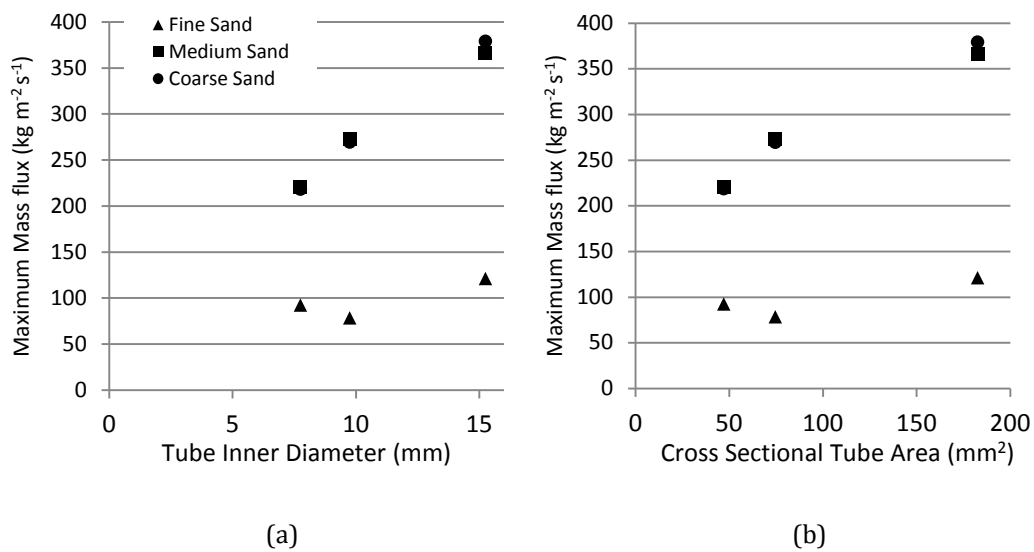


Figure 4.2. Maximum mass flux for three tube sizes and three sand grain sizes, plotted with respect to (a) diameter and (b) cross-sectional area.

A few observations can be made from the flow rate experiments. First, the mass flux values demonstrated here are up to $379 \text{ kg m}^{-2} \text{ s}^{-1}$, almost an order of magnitude higher than the maximum values considered for Particle Suspension Receiver studies ($45 \text{ kg m}^{-2} \text{ s}^{-1}$) [8]. This is valuable finding because in a final receiver design,

a low mass flux such as that of the Particle Suspension Receiver will require a much larger receiver, possibly limiting the efficiency. Second, the Medium and Coarse sands are nearly identical in their maximum flux, whereas the fine sand mass fluxes are much lower. While not tested or verified, this is likely due to the higher friction of the fine sand due to the greater number of particle-particle interactions that take place as the mixture flows. Third, mass flux not only increases with diameter of the tube, it also increases with the cross sectional area. Increasing mass flux with diameter is very intuitive, but mass flux increasing with area is a more interesting observation. Simply put, this means that if a tube has a cross sectional area of 2.0 cm^2 , it will have a mass flux *more than twice* that of a similar 1.0 cm^2 tube. Last, the one data point that does not follow the trend is the fine sand in 9.75 mm tube. Upon close inspection, a slight narrowing of this glass tube can be measured at the outlet, clearly from the glass manufacturing, which would logically result in a lowered mass flux measurement for this point alone.

It was important to establish these maximum flow rates before moving on to heated tests where an opaque copper tube rather than a transparent glass tube was used, so as to not exceed these flow rates and unintentionally switch over to the free-fall flow regime. Trends shown are nearly linear, so the maximum flow rate for any tube diameter in the range studied can be easily approximated.

4.2 Plug Flow Approximation

As shown by several other researchers, a gravity driven DGF with smooth walls is very close to a “plug flow” or “slug flow” [18] where the velocity profile is uniform. In this type of flow, the typical “no-slip” boundary condition is not followed, and instead the wall has full slip or zero wall shear stress.

Watching the flow in a glass tube, it is clear there is a high degree of slip. To quantify this and verify the plug flow approximation for the current materials, video footage was taken of sand flowing through the 7.75 mm ID glass tube with a measuring tape along the length (Figure 4.3). In sequential video frames, the locations of visible particles were recorded, which was used to calculate the average axial velocity of particles at the wall. With measurements of mass flow rate and a

known bulk density, the mean axial velocity was also calculated. Comparing these two velocities, it was found that the velocity at the wall was 90% of the average velocity, indicating a very high degree of wall slip a velocity profile that is nearly uniform.



Figure 4.3. Image of video footage used to calculate particle velocity at the wall.

4.3 Heat Transfer Experiments

Heated tests were performed with the goal of determining the heat transfer coefficient to the flowing sand. The previous setup was modified to accommodate a 14 mm ID, 1.2 m long copper tube wrapped with eight heating elements, as shown in Figure 4.4. Instead of the adjustable valve, four different orifice plates were used to achieve various mass flow rates. Seven K-type thermocouples, placed along the tube in between each of the heating elements, were firmly attached and insulated to accurately measure the outside surface temperature of the copper tube. Thermocouples were also used to measure the inlet and outlet sand temperatures.

Nominally, 2300 Watts were input to the heating elements, but a large fraction was lost to the surroundings. The setup was left uninsulated because the elements were hot enough to burn the fiberglass insulation that was originally applied. The actual

heat input was calculated with the inlet and outlet temperatures, the mass flow rate, and sand heat capacity using Equation (4.1), so the losses do not affect the final results. Upon starting each test, the setup was allowed to reach steady state before all data was recorded.

Figure 4.5 shows the external temperatures measured along the tube for various conditions. Each of the three sand types were tested, and each of the four orifice plates were used. While this would result in 12 combinations, the two larger orifice plates were not tested with the fine sand, as this leads to the free-fall flow regime, leading to 10 runs, each represented by a line in the graphs below. Flow rate through the orifice is different for each sand type, so the measured flow rate is noted in the legend.

As expected for internal flow with a uniform heat flux boundary condition, the surface temperature of the tube increases almost linearly from inlet to exit, as the interior sand heats up along the path. The relationship is not quite linear, likely because the last heating elements are at a higher temperature and therefore have higher emissive and convective losses to ambient than the first elements.



Figure 4.4. Heated copper tube with 8 heating elements.

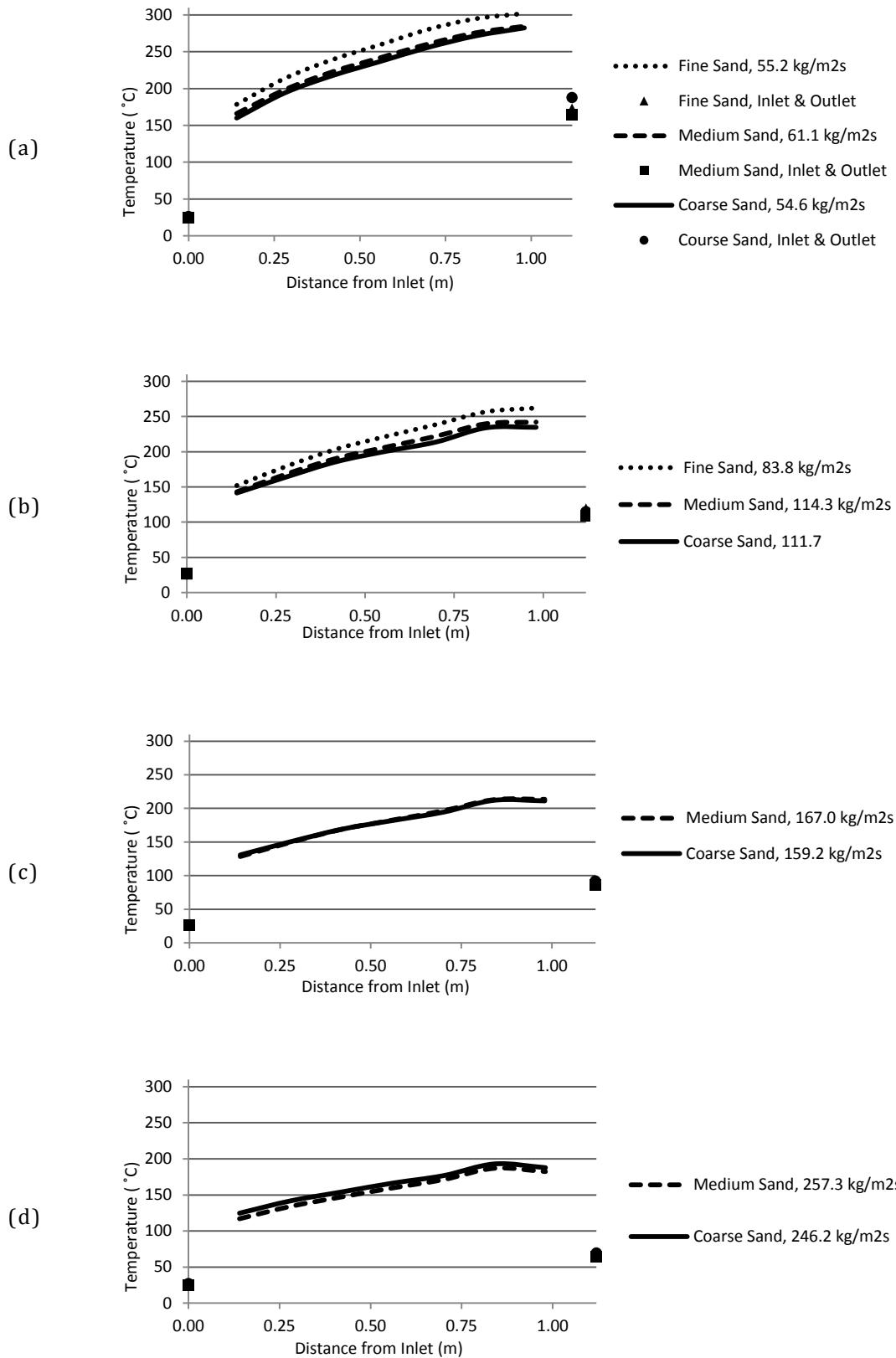


Figure 4.5. Steady state tube surface temperatures (lines) and sand inlet and outlet temperatures (icons) with four 4.75 mm orifice holes (a), one 9.4 mm orifice (b), one 11.0 mm orifice (c), and one 12.4 mm orifice (d).

For each of the 10 test runs, the heat transfer coefficient of each test was calculated, as plotted in Figure 4.6. First, Equation (4.1), noted below, was used to calculate the actual heat transferred to the sand. Heat flux was assumed to be uniform, though in reality, losses to the environment would be higher near the exit than the inlet, due to the higher surface temperatures.

$$Q = \dot{m}C_p(T_{outlet} - T_{inlet}) \quad (4.1)$$

The heat transfer coefficients were calculated with Equation (4.2) [17].

$$h = \frac{Q}{A(T_{surface} - T_{bulk})} \quad (4.2)$$

Bulk temperature is the velocity-weighted average temperature, but even in this situation where velocity is nearly uniform, it is difficult to measure experimentally at various points along the tube length. With the constant heat flux boundary condition in an internal flow, the bulk temperature rises linearly with the distance from the inlet, and once fully developed, the surface temperature rises in a similar manner [17]. Thus, the bulk temperature was calculated at each point along the tube by linearly interpolating between the inlet and outlet sand temperatures.

The area, denoted as A in Equation (4.2) above, is taken as the internal surface area of the tube. The surface temperature on the exterior of the tube was measured, but the interior surface temperature should be used in Equation (4.2). There will be a temperature gradient between the inside and outside walls of the tube, but this difference is negligible due to the high thermal conductivity of copper and the thin (1 mm) tube wall.

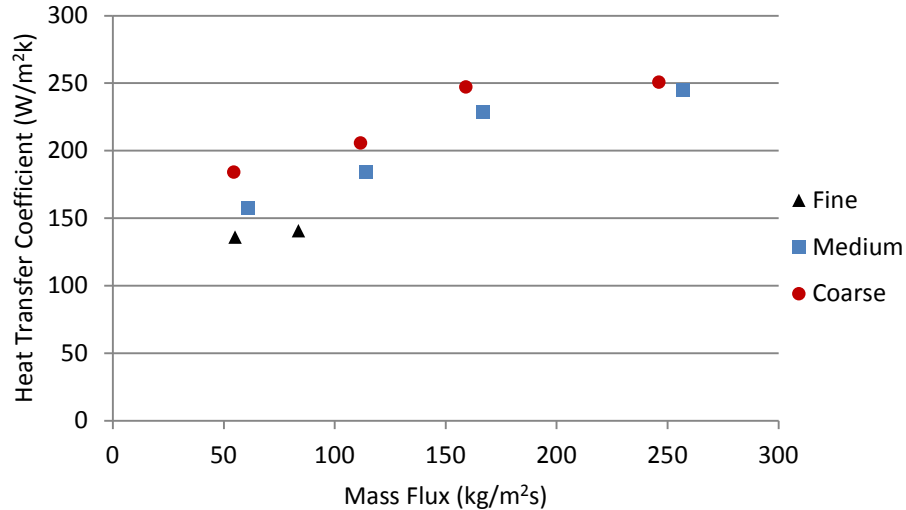


Figure 4.6. Heat transfer coefficient at various mass flux values.

The heat transfer coefficient increases with mass flux, similar to trends shown in Particle Suspension Receivers [8] and in DGF experiments [18].

The heat transfer coefficients are much lower than results presented for Particle Suspension Receivers ($400\text{-}1100\text{ W m}^{-2}\text{ K}^{-1}$) [8], which is likely due to the lower particle and air velocities in DGF. The h values are also lower than those presented in DGF research ($325\text{-}375\text{ W m}^{-2}\text{ K}^{-1}$) [12], possibly due to the ceramic particles used in that study.

4.4 Summary of Tube Experiments

From the vertical tube experiments, there are several important outcomes:

- Maintaining a dense granular flow requires a restriction at the outlet to avoid the free-fall flow regime.
- No blockages of flow or unexpected frictional effects were seen.
- Mass flux was demonstrated up to $379\text{ kg m}^{-2}\text{ s}^{-1}$ and increasing with tube diameter.
- The plug flow approximation is shown to be valid.
- Heat transfer coefficients are in the range of $130\text{ to }250\text{ W m}^{-2}\text{ K}^{-1}$, increasing with flow rate and sand grain diameter.

CHAPTER 5

EXPERIMENTS: PARALLEL PLATES

The envisioned receiver to model consists of sand flowing vertically through many rectangular channels separated by fins (Figure 6.1 in Section 6.1). The experimental setup was built to study this exact geometry: 1D heat flow in a long, thin, vertically flowing channel.

5.1 General Experimental Setup

The same hopper used in the tubular experiments was used to feed sand into the channel. The channel was formed by a steel sheet at the back, a copper sheet at the front, and strips of fiberglass to maintain a 1.0 cm spacing between the two pieces of metal. Electric resistance heater wire was wrapped around and insulated by sheets of thin glass material (Figure 5.5) before adding a second steel plate to hold the heater wire in place. Side, front, and top views are shown in Figure 5.1. The channel itself measured 11.0 cm x 1.0 cm, and the heated section was 1 meter in length.

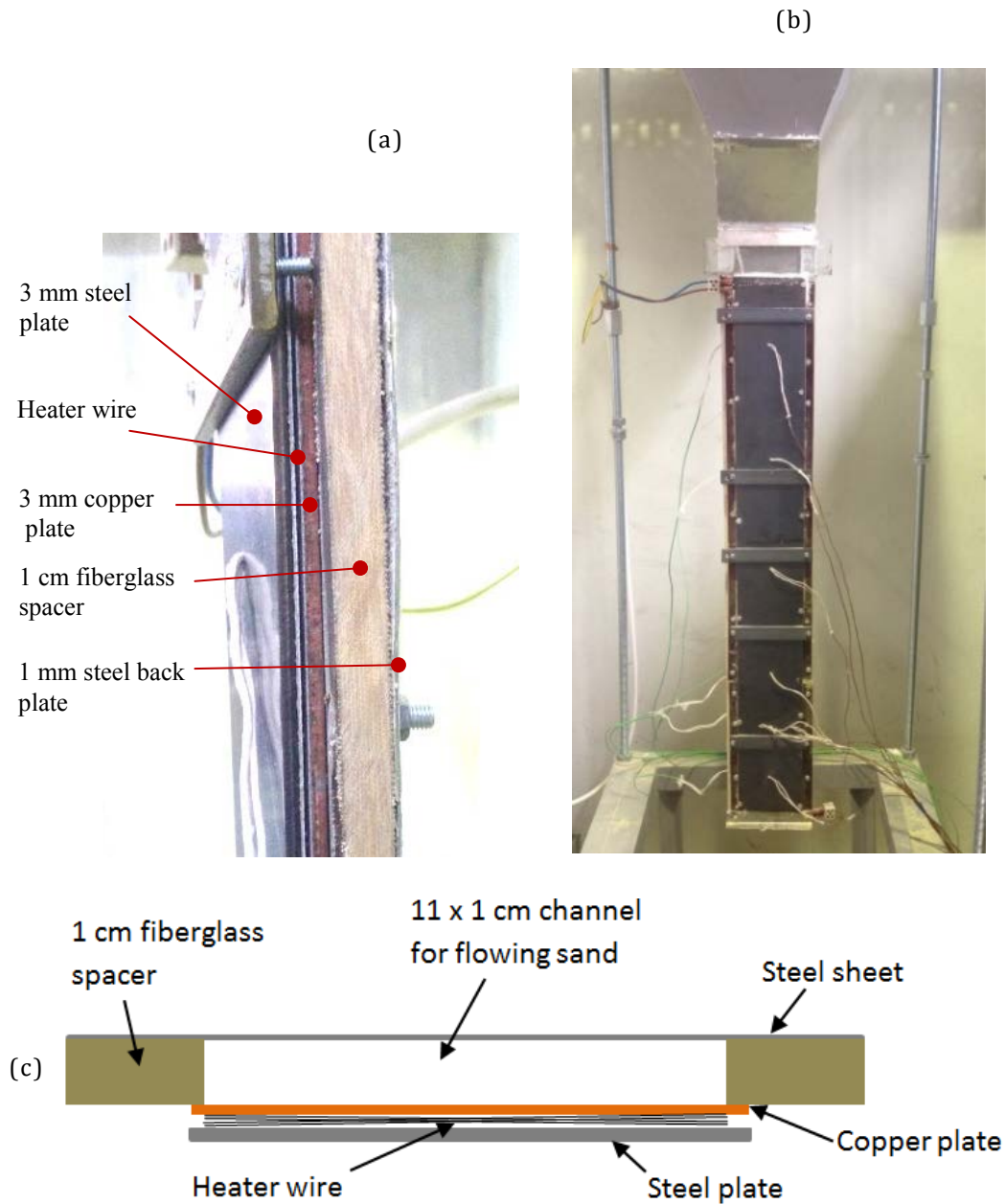


Figure 5.1. Side view of channel construction (a), front view (b), and cross section (c).

The whole setup was insulated with high temperature ceramic insulation (Figure 5.2). Above the heater, a glass window allowed for visually observing the flow when insulation was not used. A Variac controlled the power input, so different power levels and temperatures could be achieved.



Figure 5.2. Heated channel with ceramic insulation.

5.2 Flow Regulation and Measurement

An aluminum restriction plate was placed over the channel outlet to maintain a constant flow rate (Figure 5.3). The plates used a number of 5/16 inch holes, equally spaced across the 11 cm channel width. Tests were run using plates with 4 holes, 7 holes, and 10 holes. Alternatively, a valve could have been designed to adjust the flow rate more easily. However, unless designed carefully, thermal expansion during tests could change the flow restriction of the valve, changing the flow rate. The shape of the restriction plates should change negligibly with heating.

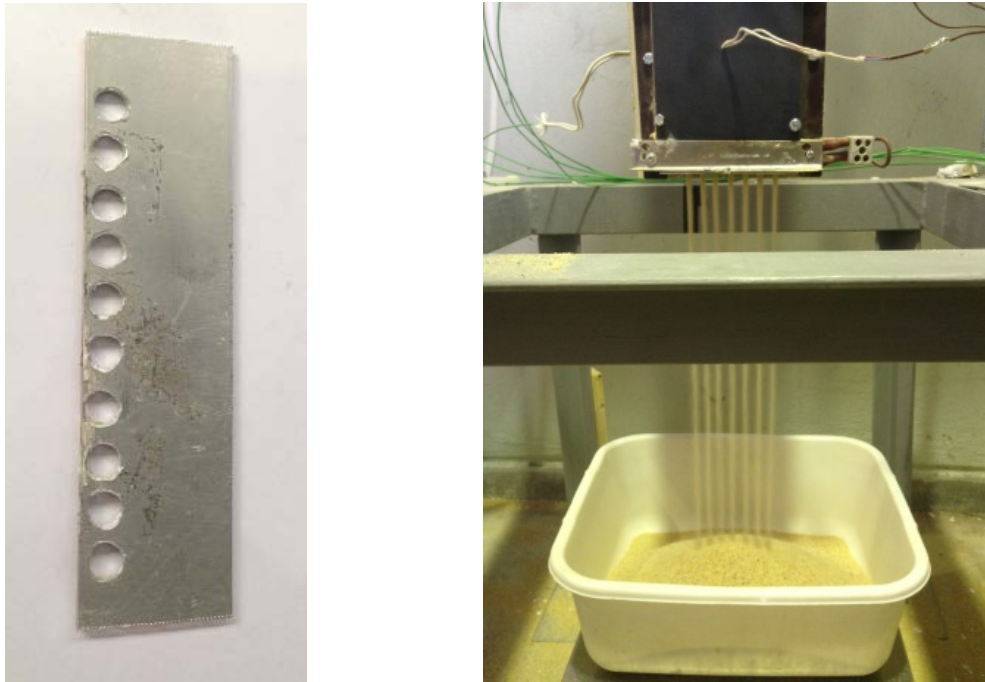


Figure 5.3. Restriction plate (left) and sand flowing from channel (right).

5.3 Heater Surface Thermocouple Attachment Method

To measure the surface temperature of the copper sheet, T-type thermocouples were attached by threading holes in the copper and securely tightening the thermocouple junction under the head of a brass screw, ensuring good thermal contact (Figure 5.4). Brass screws were countersunk to minimize any effect on sand flow.



Figure 5.4. Thermocouples measuring heated surface temperature, secured under the head of a brass screw. Fiberglass insulating sleeve in white.

To avoid having thermocouple wires passing through the flowing sand, which would certainly affect the flow, thermocouple wires were routed out through the front face of the heater, as seen in Figure 5.5 where the steel plate has been removed and heater wires can be seen. Thermocouple wires were insulated with a white fiberglass sleeve to reduce thermal conduction through the wire itself.

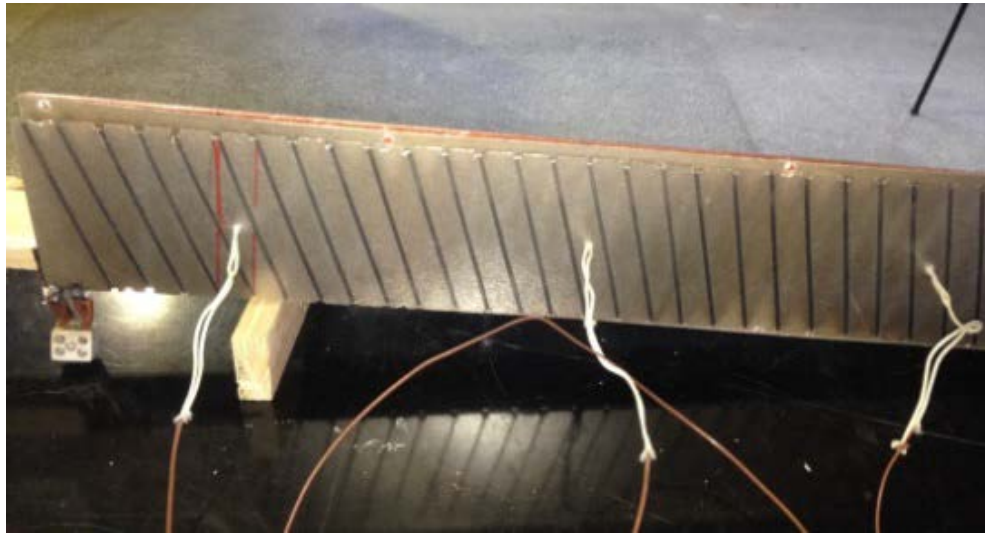


Figure 5.5. Resistance heater wire wrapped around glass material, with steel backing plate removed. Thermocouple wires pass through heater and out front face.

5.4 Thermocouple Placement

As shown below in Figure 5.6, eight thermocouples were attached to the copper heater surface. The top four have a spacing of 20 cm, whereas the spacing is decreased to 10 cm near the bottom to capture more granular data as the thermal boundary layer develops.

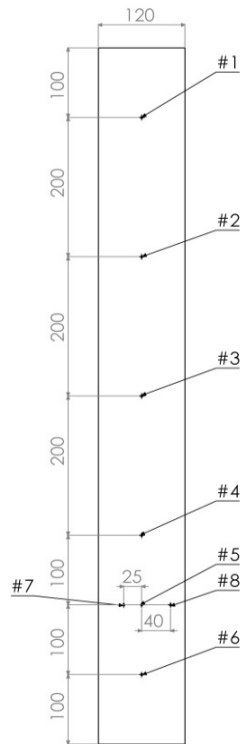


Figure 5.6. Thermocouple placement on heated copper surface, dimensions in mm.

5.5 Steps to Minimize Undesired Heat Flow

Efforts were made to ensure heat flux was applied uniformly both vertically and horizontally to the copper sheet. The original heater used a thin copper sheet, but once mounted it flexed enough in the center to measurably reduce the channel cross section, so it was replaced with a thicker 3 mm copper sheet to increase the stiffness. The steel plate acting as a backing for the heater was increased in thickness as well, and the combination led to a very stiff heater with no measurable deflection once installed.

The side spacers to enclose the sides of the channel, originally steel, were switched to fiberglass to reduce any heat transfer around the ends, which would result in a deviation from the infinite parallel plate flow problem. In addition, the contact area of the copper plate to the fiberglass spacers was kept to a minimum, 5 mm, in order to minimize any heat conduction through the fiberglass spacers.

As heat was applied to the copper surface uniformly and care was taken to minimize any conduction to the spacers, there should be very little temperature variation in the lateral direction. Thermocouples 5, 7, and 8 were used to verify this; measurements stayed within 1.0 °C across all three thermocouples during all tests, indicating any lateral non-uniformity had been eliminated.

5.6 Sand Outlet Temperature Measurements

Accurately measuring the bulk temperature of the sand at the outlet presented some challenges. Sand exiting the channel was not uniform in temperature, so a single thermocouple placed in the flow of sand could not accurately measure the bulk temperature. Using several thermocouples could be considered to measure the temperature profile of the sand, but due to the small thickness (1.0 cm) and large temperature gradient in the channel, inserting multiple thermocouples would likely prove inaccurate and would also introduce an error by restricting the sand flow.

The alternative is to mix the sand to find the bulk temperature. Using fiberglass insulation sheets, a nozzle was built to concentrate and mix the different streams leaving the orifice plate (Figure 5.7). Three different methods of measuring the bulk temperature were performed and are discussed below.



Figure 5.7. Insulating nozzle to mix and concentrate flow.

1. **Falling Particles.** A thermocouple was placed in the outflow of nozzle, in the region where sand and air are vigorously mixing as the particles fall. The thermocouple is in the air, but it is constantly bombarded by hot falling particles.
2. **Granular Flow.** A thermocouple was placed along one of the inclined surfaces inside the nozzle, very near the wall. Since the inclined edges of the nozzle are not very steep, particles are *not* in free-fall at this location. Instead, the particle stream flows downward along sloping edge in a dense flow, covering up the thermocouple with particles.
3. **Insulated Container.** Particles are collected in an insulated container (Figure 5.8), and the temperature is measured with a thermocouple inside.



Figure 5.8. Insulated container with thermocouple for measuring bulk temperature of particles.

Table 5.1. Bulk outlet temperature measured with three different methods.

Temperature Measurement Method	Run Number					
	1	2	3	4	5	6
Falling Particle	45.9	54.5	35.4	33.2	33.5	31.7
Granular Flow	42.0	48.9	47.5	43.8	37.2	34.2
Insulated Container	43.9	52.6	37.4	34.8	31.0	32.6

Table 5.1 shows six test runs with various flow rates and power input levels, and the outlet temperature for each run was measured using the three different methods. For

the same run, the three methods conclude very different temperatures. Furthermore, the deviations are not constant; in the first two runs, the Falling Particle thermocouple reads highest, but in the last four runs the Granular thermocouple is highest.

These discrepancies may be caused due to insufficient mixing. The insulated nozzle facilitates mixing of hot and cold portions of the sand, but it is still possible that full mixing is not achieved and the temperature measurement at a single point is not representative of the entire particle flow. Because of this potential inaccuracy, the Falling Particle and Granular Flow methods were not used for future calculations. In future experiments, a better nozzle should be built to accomplish complete mixing.

In the Insulated Container method, particles are collected, an insulating cap is applied, the contents are shaken, and the container is set down to come to thermal equilibrium. This method should achieve a true measure of the bulk temperature, since vigorous mixing eliminates any difference between colder and hotter portions of the particle streams. However, one source of error can be anticipated; particles fall a short distance from the nozzle into the container through room temperature air, about 10 cm, and they lose heat as they fall due to convection. Since the particles have a very high surface area to volume ratio, convection will quickly affect the particle temperature. Given the shortcomings of the various methods, the Insulated Container method is chosen to be the most accurate measure of the bulk temperature and is used in the calculations that follow.

5.7 Sample Results

Data logging, in 10 second increments, was started when the sand flow and power input were started, but only steady state values were desired for calculations. When the relative change between data points reached an equivalent of 1 °C per 5 minutes, the system was considered at steady state. Figure 5.9 shows the transient heat-up for the copper surface thermocouples. Steady state was reached after running for roughly one hour.

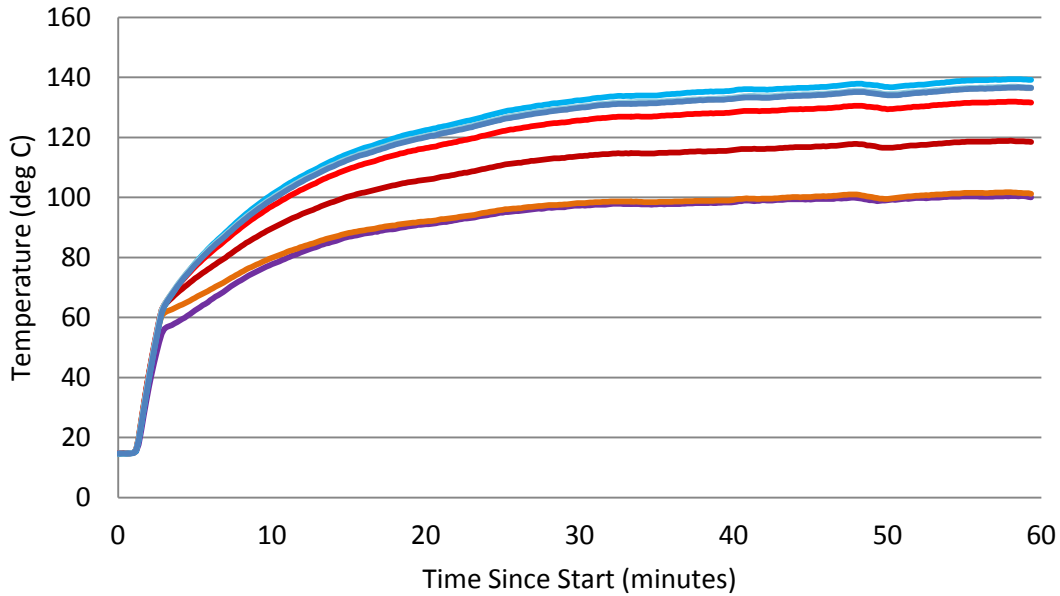


Figure 5.9. Transient response of heated surface temperatures.

Steady state temperature results are obtained such as those presented in Figure 5.10. The two inlet temperatures are nearly identical, so one is not visible. In these experiments, Tests 1 and 2 had nominal power inputs of 471 and 613 watts respectively, and they have nearly identical flow rates. It matches expectations that the surface temperatures of Test 2 are higher than Test 1, and a greater increase in temperature is seen from inlet to outlet.

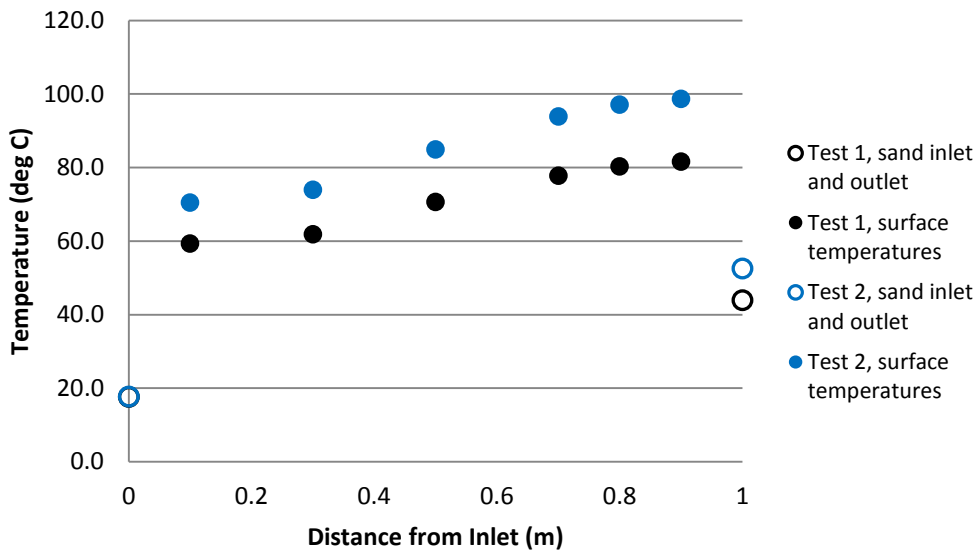


Figure 5.10. Sample data showing heated surface temperatures and bulk inlet and outlet temperatures.

5.8 Analysis of Experimental Results

For an internal flow with a constant heat flux boundary condition, the shape of the temperature profile is constant once thermally fully developed, meaning all temperatures rise *linearly* with the distance from the inlet at the same rate [17]. The temperature rise per unit length, dT/dx , can be found from the slope of the heated surface temperatures. Once the surface temperature becomes linear, fully developed conditions have been established.

For demonstration of these trends, the 11 cm x 1 cm x 1 meter channel was modeled in ANSYS Fluent. The heated surface was given a uniform heat flux, and all other surfaces were given adiabatic boundary conditions. Figure 5.11 shows the surface temperatures of the heated and insulated walls, and it is clear that after an entrance length of about 0.4 meters, the temperature of each surface increases linearly along the channel. A trend line was added to the data points representing the fully developed region, and the equation of each data set is shown. The slope, dT/dx , is nearly the same for the heated and insulated surfaces as expected.

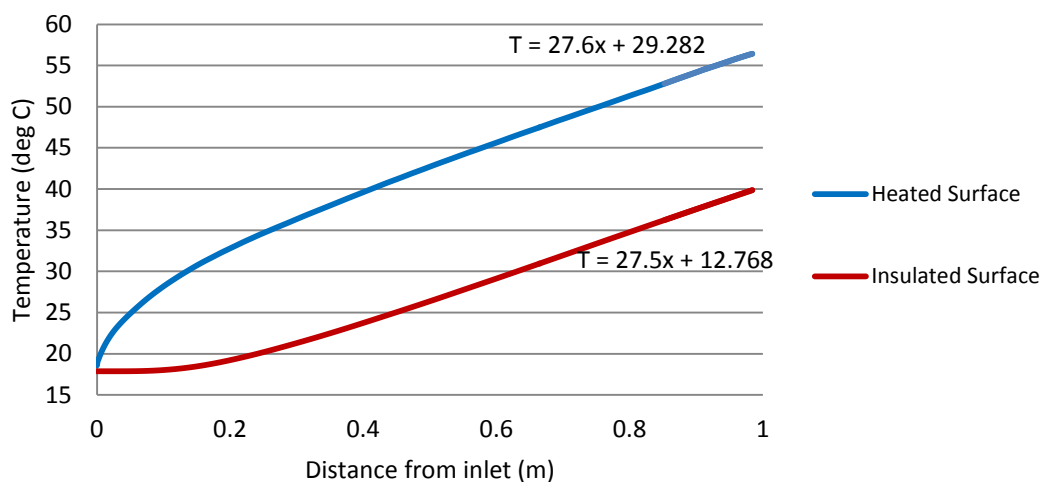


Figure 5.11. Heated and insulated surface temperatures parallel plate flow reaching a fully developed region state.

Comparing Figure 5.11 to Figure 5.10, there are some differences in the trends. In the modeled version, the heated surface temperature, bulk sand temperature, and insulated surface temperature are all equal at the inlet. In contrast, the experiment shows a large difference between the bulk sand inlet temperature and the heated

surface temperature near the inlet. The surface temperature at the inlet was not actually measured, but from the trend it is expected to be much higher than the bulk inlet temperature. Furthermore, the experimental data shows the slope approaching linearity, but it is not quite achieved. These significant differences indicate something was incorrect with the execution of the experiment or the assumptions of the model. These trends would fit a case where the heat flux was not actually uniform, so it is hypothesized that the 3 mm copper sheet was conducting a significant amount of heat in the vertical direction. The temperature of the copper sheet was lowest near the inlet, so heat would be conducted in that direction, and the heat flux to the sand would actually be higher near the inlet than the outlet.

To investigate the effects of heat conduction through the copper sheet, a 3 mm copper sheet was added to the Fluent model. Figure 5.12 (a) shows the model with a uniform heat flux boundary condition applied directly to the flowing sand, whereas Figure 5.12 (b) uses a heat flux boundary condition applied to a 3 mm copper plate which contacts the sand. In (b), as seen in the experimental data, the heated surface temperature at the inlet is significantly higher than the insulated surface temperature, and the heated surface does not appear to approach a linear profile. Thus, it is clear that conduction within the copper plate is preventing the uniform heat flux boundary condition from being implemented correctly, and it prevents any analysis based on this assumption.

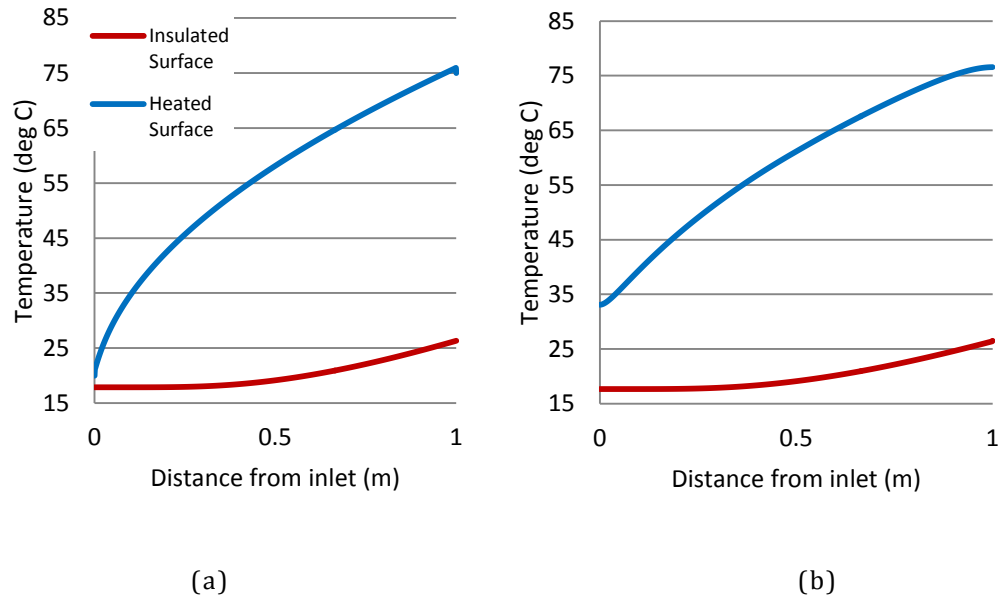


Figure 5.12. Uniform heat flux boundary condition applied directly to sand (a), and uniform heat flux applied to a copper plate which contacts sand (b).

5.9 Calculation of k_{eff} in the Fully Developed Region

The goal is to classify, through experimentation, how heat transfers to the flowing sand, which is typically characterized by a heat transfer coefficient (h). The heat transfer coefficient can be found experimentally as in the tubular experiments using Equation (4.2). However, a heat transfer coefficient *cannot* be directly implemented in CFD modeling at the interface between two domains in a conjugate heat transfer problem. Specifying a heat transfer coefficient is common for a boundary condition, that is, on the *edge* of the problem domain. However, it cannot be applied at the *interface* of two domains (in this case, at the solid and “fluid” sand mixture interface). This is because CFD code will calculate the heat transfer based on the fluid properties including thermal conductivity, viscosity, and density. Therefore, specifying the heat transfer coefficient (or any other boundary condition) in between the two domains over-defines the problem.

If a uniform heat flux were actually applied, as originally planned, the heat transfer properties could be found with the method presented in this section. Since this is not the case, the properties must be found through the method in the next section, which focuses on the behavior in the entrance region. Future experiments will ensure a

uniform heat flux will be applied to the sand, and k_{eff} will be determined in the fully developed region described here.

Since CFD modeling requires the thermal conductivity of the fluid as an input instead of h , a value of effective thermal conductivity, k_{eff} , can be chosen that will deliver an equivalent heat transfer. Modeling can then proceed with k_{eff} of the fluid, and h is no longer needed. Under hydrodynamically and thermally fully developed internal flow conditions, the Nusselt number (Equation (5.1)) is constant, leading to a linear relationship between h and k_{eff} [17]. Stated another way, h is a function of only k . After finding the k_{eff} value which matches the experimentally found heat transfer, CFD modeling can be simplified from a complex multi-phase problem to a single-phase, plug flow problem.

$$Nu_D = \frac{hD_h}{k} \quad (5.1)$$

Nusselt number for fully developed flow between two flat plates, heated on one side and insulated on the other, is widely given as 5.39 [14, Table 8.1]. However, this derivation assumes a no-slip boundary condition, resulting in a parabolic velocity profile, which is not the same as the current case of a uniform velocity profile. Instead, a Nusselt number of 6.0 should be used for plug flow conditions, which is derived in Appendix B and corroborated by others [24]. To find h from experimental data, Equation (4.2) is used again, at a single point in the fully developed region. Details of the parameters are discussed below.

T_{surface}. The heated surface temperature is measured directly.

Heat flux, Q/A. With the total power input measured by the Variac, a surface area of 0.11 m², and the assumption that heat flux is uniform, a heat flux can be calculated. This would ignore any heat lost to the environment, so it would overestimate the heat flux. While losses were not calculated or modeled in this study, they are expected to be quite low, as the external insulation temperature was not noticeably different from the surrounding air temperature. The other method to find the total heat transfer, which incorporates any losses, is to use the temperature rise from inlet to outlet, using Equation (4.1). A similar method was used in the

tubular experiments. However, both of these methods assume that heat is transferred to the sand uniformly, which is not true for this experimental setup as previously described.

T_{bulk} . The bulk temperature at a location inside the channel is difficult to measure directly, so it must be calculated from available data points. With the uniform heat flux boundary condition, bulk temperature always rises linearly along the channel, and once fully developed the surface temperature does as well, at the same rate. Mathematically, dT/dx is constant, where x is the direction of flow. With dT/dx easily calculated from the surface temperatures, the bulk temperature can be interpolated at a distance from the exit with Equation (5.2).

$$T_{\text{bulk},(\text{outlet}-\Delta x)} = T_{\text{bulk},(\text{outlet})} - \frac{dT}{dx} \Delta x \quad (5.2)$$

5.10 Calculation of k_{eff} in the Entrance Region

Given that the copper conduction in the heater plate eliminates the option of reaching fully developed flow and using the Nusselt number to find k_{eff} , a non-uniform heat flux boundary condition must be assumed and heat transfer must be studied in the entrance region. This was done by incorporating the 3 mm thick copper plate into the CFD model and varying the conductivity of the sand until the CFD results match the experimental values.

Each experimental run was modeled in Fluent after applying the relevant parameters measured during experimental testing, including mass flow rate, power input, and sand inlet temperature. After tailoring the CFD model to specific test run, the solution was obtained with various thermal conductivity values, as shown in Figure 5.13. Comparing the experimental and simulation results, the overall trends match, with deviations largest near the inlet and exit regions. The cumulative percent error between experimental and simulation surface temperatures was found for each k value. The most accurate value for k_{eff} was taken to be the one with the minimum total error. Figure 5.13, shows simulation results plotted for several k values, and k_{eff} was determined to be $0.26 \text{ W m}^{-1} \text{ K}^{-1}$.

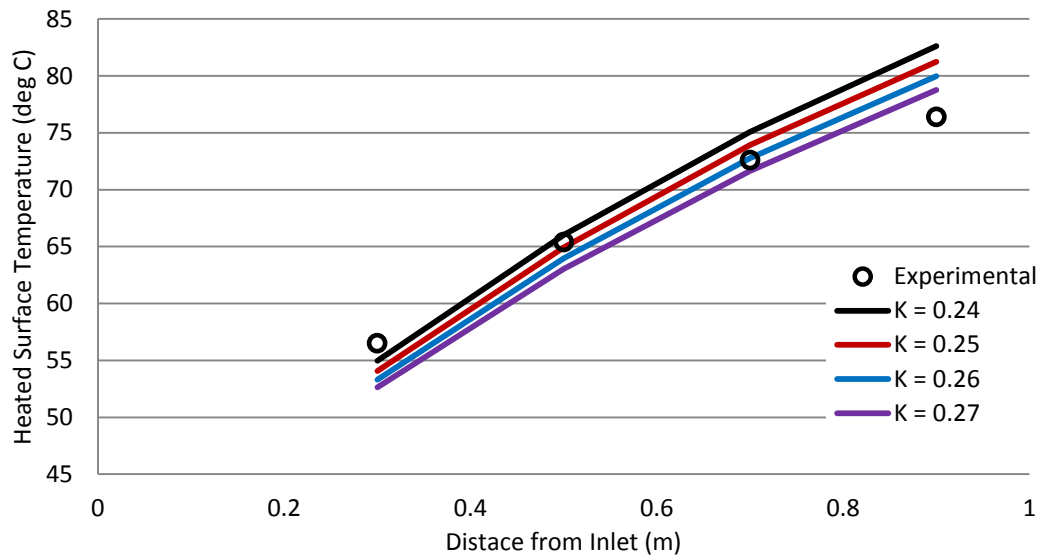


Figure 5.13. Heated surface temperatures, showing experimental and modeled results with various thermal conductivity values.

During several tests, thermocouple #1, at a distance of 0.1 m from the inlet, gave faulty readings which could not be used, so these were not included in the analysis and not shown in Figure 5.13. In addition, to keep the relative weight of errors the same, the data points must be equally spaced, so thermocouple #5 at 0.8 m from the inlet was not included in the error calculations leading to the prediction of k_{eff} .

5.11 Results and Discussion on k_{eff}

Experimental runs were conducted at various flow rates and power input levels, and the k_{eff} values were determined. Results are presented for the six runs in Table 5.2 below.

Table 5.2. k_{eff} values calculated by matching experimental data to Fluent modeled results.

Run Number	Restriction Plate	Mass flow rate (kg s ⁻¹)	Average Velocity (cm s ⁻¹)	Heat Flux (W m ⁻²)	Calculated k_{eff} (W m ⁻¹ K ⁻¹)
1	4 holes	0.021	1.23	3842	0.25
2	4 holes	0.021	1.23	5090	0.27
3	7 holes	0.035	2.07	5593	0.25
4	7 holes	0.035	2.06	4869	0.26
5	10 holes	0.051	3.03	6200	0.24
6	10 holes	0.046	2.72	6034	0.26

Unlike results from the heated tube experiments, heat transfer cannot be easily correlated to flow velocity with these results. However, a very limited range of flow rates were considered here, between 1.23 and 3.02 cm s⁻¹, whereas the tubular tests were conducted between 3.4 and 17.2 cm/s. It is still predicted that at greater flow rates the heat transfer coefficient and k_{eff} would increase based on tubular test results and trends presented in other experimental studies [25][18]. In the future, a wider flow rate range will be considered, but currently the range was limited by the quantity of sand available given the long time it must run to achieve steady state conditions. Optimally, the relationship between velocity and k_{eff} would be found, and this would be used as an input for modeling the full receiver. However, in order to proceed with a full receiver model given the data currently available, k_{eff} was assumed to be constant with respect to velocity, and the average k_{eff} value over the six runs of 0.255 W m⁻¹ K⁻¹ was used in modeling, which is a conservative assumption.

k_{eff} is also expected to increase with temperature due to the increasing thermal conductivity of air and radiation effects. The thermal conductivity of air increases from 0.0263 W m⁻¹ K⁻¹ at 27°C to 0.0715 W m⁻¹ K⁻¹ at 827°C.[17] In a Particle Suspension Receiver the heat transfer coefficient increased almost 30% with a temperature increase from 220°C to 580°C [8]. Radiation is expected to be

negligible below 400°C, but it will play an important role in the bulk conductivity above this temperature for fluidized flows [26]. In the low temperature range studied here, no relation between k_{eff} and temperature can be found, so modeling proceeded assuming k_{eff} is not a function of temperature, which is also a conservative assumption.

Examining the trajectory of the experimental and modeled surface temperatures (Figure 5.13), the CFD-modeled surface temperatures appear to be trending higher than the experimental values at locations greater than one meter, meaning the value of k_{eff} would have been calculated higher if a longer experimental test section was used. It is unclear why the experimental and CFD data do not match over a longer section, but 0.255 W m⁻¹ K⁻¹ was chosen (again, a conservative value) so modeling could proceed. Future experiments should use a longer section, ideally as long as an actual receiver.

Baumann and Zunft [27] modeled k_{eff} of static sand based on the properties of the constituent materials, showing values from 0.24 W m⁻¹ K⁻¹ at room temperature up to 0.63 W m⁻¹ K⁻¹ at 800 °C. The static k_{eff} at room temperature very closely matches the k_{eff} for flowing sand found in this thesis, showing that the flow has done little to enhance heat transfer at the low flow rates tested. Nonetheless, this verifies that k_{eff} calculated here is in the correct range.

In another study, k_{eff} was presented by Sullivan [20] as 0.2 Btu hr⁻¹ ft⁻¹ °F⁻¹ (0.35 W m⁻¹ K⁻¹) for fine sand flowing in the critical (slowly flowing) state, though no details were given on the method of calculation.

CHAPTER 6

MODELING OF THE RECEIVER

6.1 Overview

Modeling the finned receiver with sand flow is an example of “conjugate heat transfer”, where more than one material must be modeled simultaneously to correctly solve the heat transfer problem. In this case, the metal receiver receives heat and transfers it to the flowing sand mixture. The finned receiver is depicted in Figure 6.1 to show the overall heat flows modeled, and a close-up view of a CAD model is shown as well. Concentrated radiation is incident upon the receiver surface (also called the absorber), where some energy is immediately lost as a reflection. Heat is transferred to the fins and passes into the sand, which flows vertically through the open channels. Heat is lost to the environment through convection and radiation to the surroundings, which are functions of the absorber temperature. An efficient receiver would keep the surface temperature of the absorber low, close to the sand mixture temperature, limiting the losses to the environment.

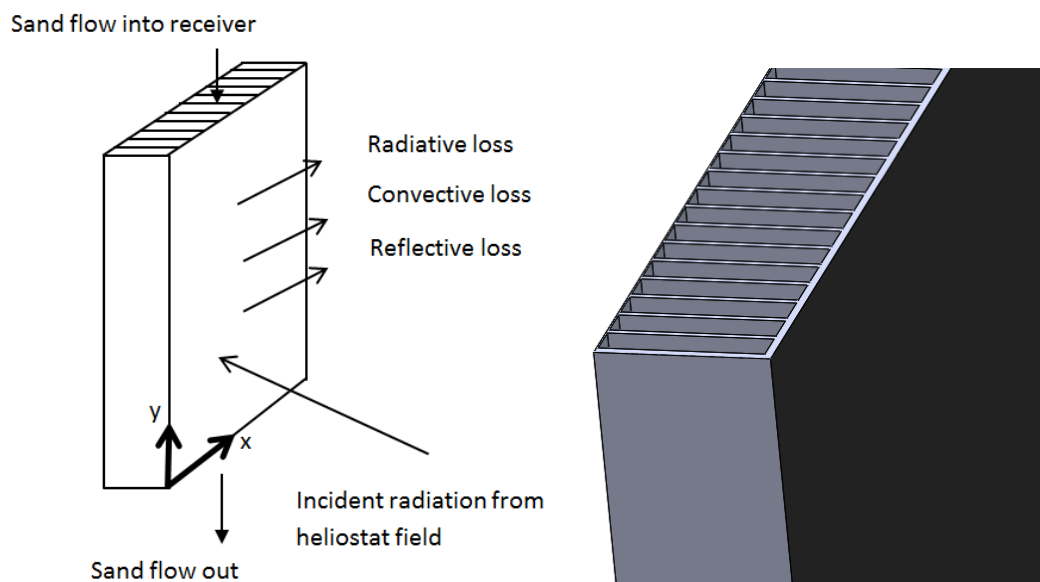


Figure 6.1. Heat flows to and from receiver (left), and corner of the finned receiver (right).

The receiver chosen to model is 5 by 5 meters, which would be considered relatively small for a utility scale power plant. Modeling the entire receiver would be extremely computationally expensive, so it was broken up into finned sections based on symmetric lines at the center of the fin and center of the flowing sand section, as shown in Figure 6.2 (a). Figure 6.2 (b) shows the 5 meter long fin once symmetry is applied, with gray representing metal and clear representing the flowing mixture.

In reality, the heat flux distribution on the surface of the receiver is not uniform, so the symmetry lines drawn do not represent perfect symmetry, but since the width of each fin is very small compared to the distribution of heat flux over the receiver, they are assumed to be symmetric. Also, there will be some conduction from the hotter central region to cooler peripheral regions of the absorber, but for the ability to consider each fin individually, conduction effects over the width of the receiver (x-direction, Figure 6.1) were neglected.

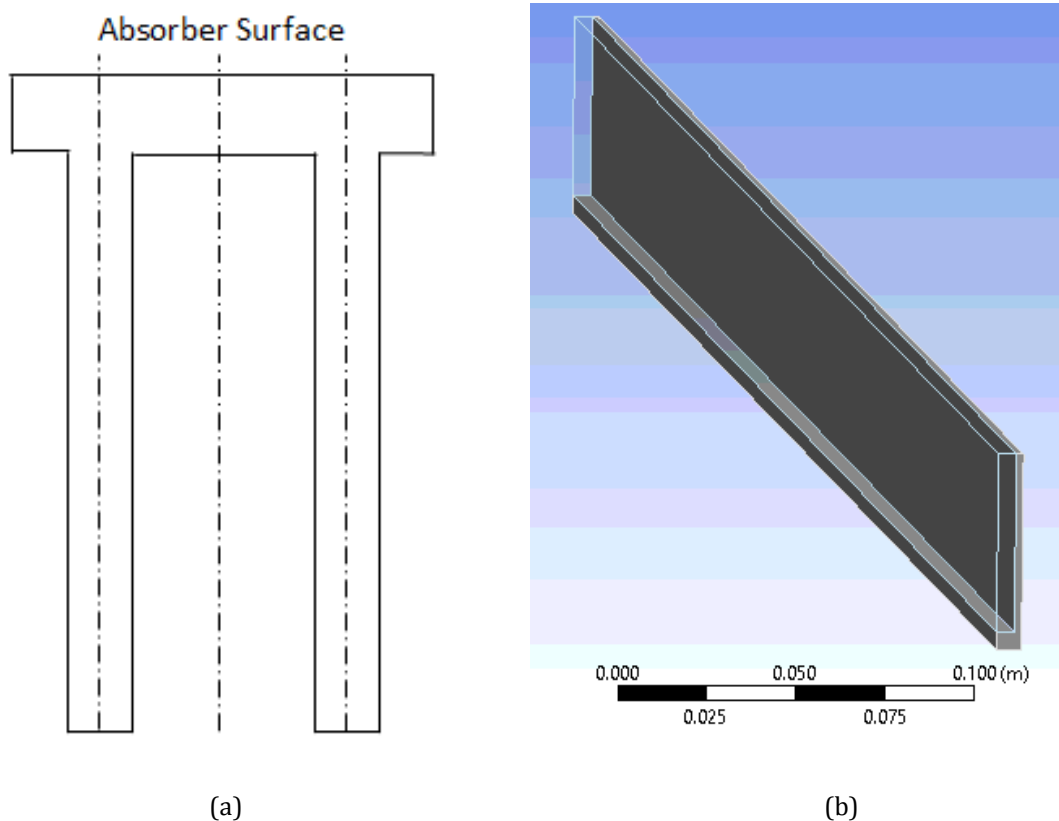


Figure 6.2. Fin cross section showing symmetry lines (a) and single fin used for CFD modeling (b).

The material chosen for the receiver was Nickel 201, with properties published by the manufacturer, Special Metals [28]. Nickel 201 was chosen for its exceptionally high thermal conductivity of $79.3 \text{ W m}^{-1} \text{ K}^{-1}$, and high melting temperature of $1435 \text{ }^\circ\text{C}$. The thermal conductivity at elevated temperatures was not given, so a constant value was used. Table 6.1 shows the parameters used for modeling.

6.2 Governing Equations

The fluid was modeled as a single phase in the laminar flow regime, under steady state conditions. SIMPLE pressure-velocity coupling was used, and momentum and energy were each discretized with second order upwinding schemes.

The equation for conservation of mass, given by Fluent, is shown in Equation (6.1).

$$\frac{\partial \rho}{\partial t} + \nabla \cdot (\rho \bar{v}) = S_m \quad (6.1)$$

Conservation of momentum is given with Equation (6.2). The stress tensor, represented by τ , is given in Equation (6.3).

$$\frac{\partial}{\partial t}(\rho \bar{v}) + \nabla \cdot (\rho \bar{v} \bar{v}) = -\nabla p + \nabla \cdot (\bar{\tau}) + \rho \bar{g} + \bar{F} \quad (6.2)$$

$$\bar{\tau} = \mu \left[\left(\nabla \bar{v} + \nabla \bar{v}^T \right) - \frac{2}{3} \nabla \cdot \bar{v} I \right] \quad (6.3)$$

The energy equation solved by Fluent is given in Equation (6.4).

$$\frac{\partial}{\partial t}(\rho E) + \nabla \cdot (\bar{v} (\rho E + p)) = \nabla \cdot \left(k_{eff} \nabla T - \sum_j h_j \bar{J}_j + (\bar{\tau}_{eff} \cdot \bar{v}) \right) + S_h \quad (6.4)$$

6.3 Boundary Conditions

The most complex boundary condition is on the absorber surface, consisting of the four heat fluxes discussed below.

- A) Incident radiation.** In actual receivers, incident radiation is concentrated in the center due to the focusing of the heliostat field. In the results that follow, first a uniform radiative flux on the receiver is assumed, and then a concentric flux is studied.
- B) Reflective loss.** Assuming the absorber surface is covered with Pyromark 2500, a typical receiver paint, absorptivity is 0.965 [29], meaning 3.5% of incident radiation is immediately lost.
- C) Radiative loss.** The absorber surface radiates heat to the surroundings at a rate defined by Equation (6.5) [17] where epsilon is the surface emissivity (0.87 for Pyromark 2500) [29] and sigma is the Stefan Boltzmann constant of $5.67 \times 10^{-8} \text{ W m}^{-2} \text{ K}^{-4}$.

$$q'' = \epsilon \sigma (T_{\text{absorber}}^4 - T_{\text{surroundings}}^4) \quad (6.5)$$

- D) Convective Loss.** Siebers et al. [30] studied experimentally the convection losses from the Solar One CSP plant in Barstow, California. A wind histogram presented shows the time distribution of wind speeds at that location, at a tower height of 78.6 meters. A mean wind speed of 7.2 m/s was found, corresponding to a convection coefficient of $21 \text{ W m}^{-2} \text{ K}^{-1}$ [30]. The receiver studied was cylindrical, so the value given is an average convection coefficient over the circular perimeter. The true convection coefficient on a flat receiver would depend on whether the wind was head-on or side-on, but a cylinder incorporates both directions, so $21 \text{ W m}^{-2} \text{ K}^{-1}$ is taken to be an average value.

The absorber surface has a complex boundary with all of the above conditions present on one surface, which is not a set of boundary conditions readily available in Fluent. A User Defined Function (UDF) was written to model this boundary condition, shown in Appendix A. The incident radiation can be set in the UDF to be a constant, as used in Section 6.5.1 to model the receiver under a uniform radiative

flux assumption. Alternatively heat flux can be set to a function of spacial coordinates as used in Section 6.6.1. In addition to applying the correct boundary condition, the UDF writes a text file with the temperature and the quantity of heat reflected, convected, and emitted from each cell on the boundary. Further post-processing analysis was performed in Matlab to find summations, maxima, minima, and average values.

The velocity at the inlet was specified with a “velocity inlet” boundary condition. With the plug flow assumption, all fluid-solid boundaries were set to zero shear stress, giving the fluid a uniform velocity profile. With no shear stress, the viscosity plays no part in the solution and is therefore arbitrary. Symmetry boundaries were used at the center of the fin and center of the flowing section, and all other boundaries were set to adiabatic walls. Table 6.1 summarizes the parameters used for modeling.

Table 6.1. Parameters used for modeling receiver.

Parameter	Value	Units	Source
Bulk density, sand	1537	kg m ⁻³	Measured
Density, Nickel 201	8890	kg m ⁻³	[28]
Specific heat, sand	776	J kg ⁻¹ K ⁻¹	[22]
Specific heat, Nickel 201	456	J kg ⁻¹ K ⁻¹	[28]
Effective Thermal Conductivity, sand	0.255	W m ⁻¹ K ⁻¹	Experimentally determined (Sections 5.9-5.11)
Thermal conductivity, Nickel 201	79.3	W m ⁻¹ K ⁻¹	[28]
Melting temperature, Nickel 201	1435	°C	[28]
h , absorber to environment	21	W m ⁻² K ⁻¹	[30]
Ambient temperature	20	°C	Assumed
Absorber emissivity	0.87	-	[29]
Absorber absorptivity	0.965	-	[29]

6.4 Mesh Independence Study

A mesh independence study was conducted to verify that results did not change with mesh size. Table 6.2 below shows the difference between the two mesh sizes studied, which was performed on configuration C (dimensions given in next section). The two mesh sizes show only 0.19 °C difference in outlet temperature, indicating the mesh is sufficiently refined. A cross section of each mesh is shown below in Figure 6.3.

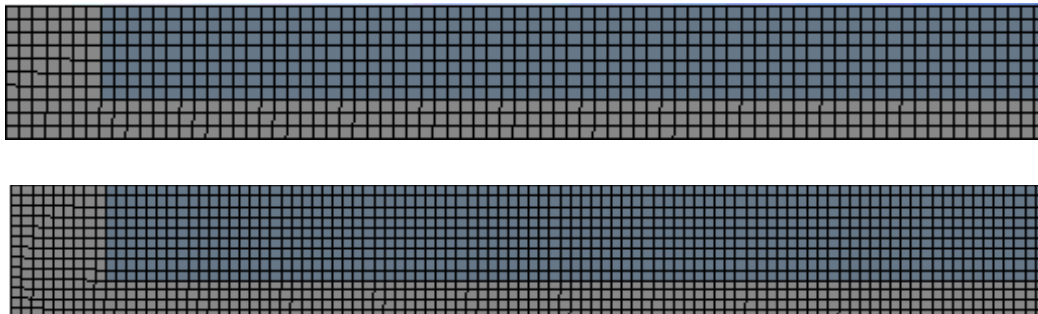


Figure 6.3. Cross section view of fin (gray) and sand (blue) with Mesh 1 (top) and Mesh 2 (bottom).

Table 6.2. Mesh size effect on outlet temperature.

Parameter	Mesh 1	Mesh 2	Difference
Number of elements	5.57E+06	1.18E+07	
Min face area (mm ²)	0.467	0.275	
Max face area (mm ²)	0.509	0.308	
Inlet temperature (°C)	500.00	500.00	
Outlet temperature (°C)	714.02	714.21	0.19

Conservation of energy was also checked for each mesh, with the results in Table 6.3 below. Both mesh sizes obey conservation of energy very well, with an overall discrepancy of less than 1 watt. A discrepancy of 6.39 watts was found between the two mesh sizes, which is still extremely small in comparison to the magnitude of the heat passing through the surface.

Table 6.3. Verification of conservation of energy.

Surface	Power Crossing Surface (W)			
	Mesh 1	Mesh 2	Difference	Percent Difference
Absorber	6381.5	6387.9	6.39	0.10%
Inlet	14163.4	14163.4	0	0.00%
Outlet	-20545.3	-20550.8	-5.47	0.03%
Net	-0.365	0.55	-	

Conservation of mass was also obeyed, with nearly no difference found between inlet and outlet for both mesh sizes. With conservation of energy and mass obeyed, and mesh size shown to be sufficiently refined, Mesh 1 was chosen to keep computing time to a minimum.

6.5.1 Receiver Modeling with Uniform Radiative Flux

If the radiative flux onto the receiver is assumed to be uniform, only a single fin must be modeled, as all fins have the same boundary conditions and will behave identically. Under this assumption, various fin configurations can be studied and compared easily. In the next section, a non-uniform radiative heat flux is considered, so each fin across the receiver has a different boundary condition, and many fins must be studied to accurately model the entire receiver.

Many different fin geometries could be considered, and an optimization could be made to find the best fin geometry for a given set of design conditions. However, within the scope of this thesis only four different fin geometries were considered, with the cross sections shown in Figure 6.4. Each fin considered was 5 meters long. Figure 6.5 (a) shows a 3D view of configuration C, where sand flows vertically down between the fins. Figure 6.5 (b) shows the fin as it was modeled after reducing the problem with planes of symmetry.

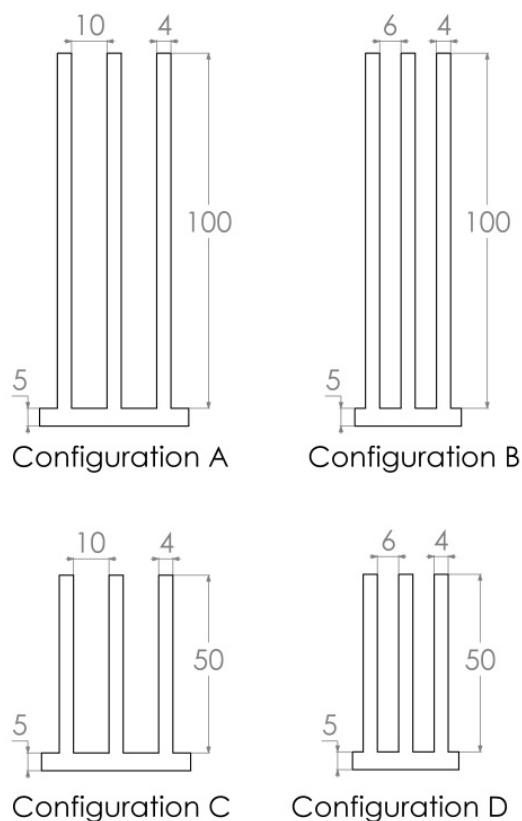


Figure 6.4. Cross sections of 5 meter long fins modeled with uniform radiant heat flux assumption, dimensions in millimeters.

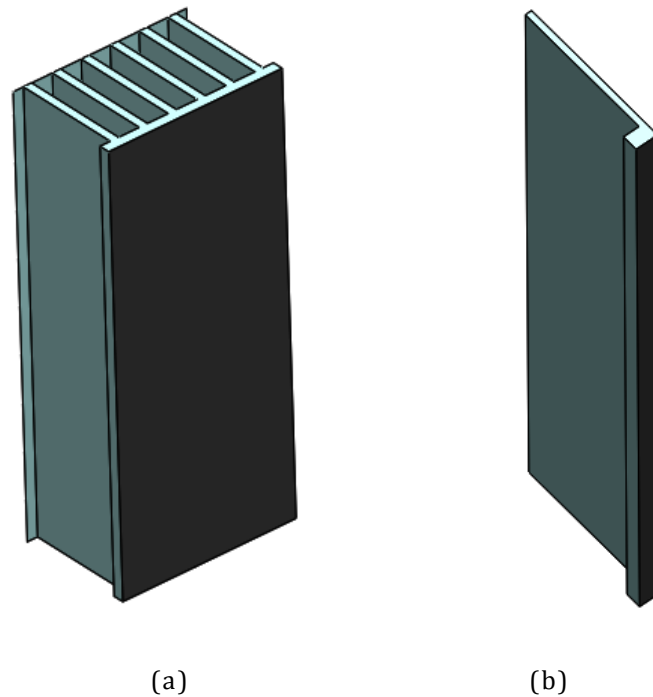


Figure 6.5. (a) Fin configuration C shown in 3D, and (b) fin modeled in Fluent after reducing the problem with planes of symmetry.

Incident flux was modeled at 300 and 600 kW m⁻². The value of 300 kW m⁻² was based on the range of 200 to 400 kW m⁻² tested on other indirect receivers [7], and 600 kW m⁻² was chosen to show results at higher flux levels which would be desirable in a real receiver. To easily compare data, the inlet and outlet temperatures should be the same for all runs. 500°C was chosen for the inlet temperature, and the flow rate was varied iteratively until the average outlet temperature was 800°C. These temperatures were chosen to reflect the high proposed working temperature of solid particle systems.

6.5.2 Results and Discussion for Uniform Radiative Flux

Heat gain and losses for the 5 by 5 meter square receiver are shown in Table 6.4 below, assuming a uniform radiation distribution and inlet and outlet temperatures of 500 and 800°C. Figure 6.6 shows these data as a percentage of incident radiation, and

Table 6.5 shows the temperature and efficiency for each configuration. As expected at these high temperatures, and as seen in other research [31], emission is by far the largest contributor to loss.

Table 6.4. Heat gains and loss from a 5x5 meter receiver, with four fin configurations and two uniform radiative flux values studied.

Config-uration	Incident Rad. Flux (kW m⁻²)	Velocity (cm s⁻¹)	Incident Rad. (kW)	Refl. Loss (kW)	Conv. Loss (kW)	Emiss. Loss (kW)	Net Heat Gain (MW)
A	300	3.10	7500	262	487	2801	3.9
	600	6.30	15000	525	616	5823	8.0
B	300	4.25	7500	262	452	2246	4.5
	600	8.90	15000	525	559	4320	9.6
C	300	6.60	7500	262	473	2566	4.2
	600	13.70	15000	525	593	5191	8.7
D	300	9.00	7500	262	432	1964	4.8
	600	19.30	15000	525	528	3606	10.3

Table 6.5. Absorber temperatures and thermal efficiency for the eight cases.

Config-uration	Incident Rad. Flux (kW m⁻²)	Max Absorber Temp (°C)	Mean Absorber Temp (°C)	Thermal Efficiency
A	300	1046	948	52.7%
	600	1298	1193	53.6%
B	300	994	881	60.5%
	600	1212	1085	64.0%
C	300	1025	921	56.0%
	600	1267	1149	57.9%
D	300	959	843	64.6%
	600	1151	1025	68.9%

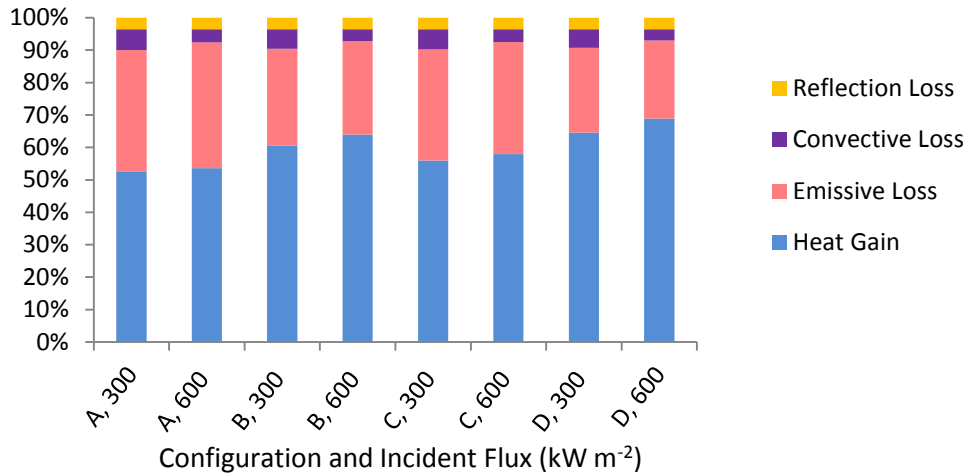


Figure 6.6. Heat gains and losses as a percentage of incident radiation.

By comparing efficiencies of A to B and C to D, it is clear that the thinner 6 mm channel leads to a significantly higher efficiency. This can be attributed to the relatively low effective thermal conductivity of sand, which does not easily conduct heat to the interior of the thicker flowing section, as seen below in Figure 6.7 below. The optimal receiver would minimize the temperature difference between the coldest part of the sand and the receiver surface, as keeping the absorber surface temperature as low as possible is the key to limiting thermal losses. Both of the plots below have an average temperature of 800°C, but configuration C has a much higher surface temperature leading to a lower efficiency, whereas the temperature in configuration D is confined within a much smaller range. Clearly, one key to an efficient design is to minimize the depth of any section of flowing sand, and in the future a parametric study of fin width and spacing could be performed.

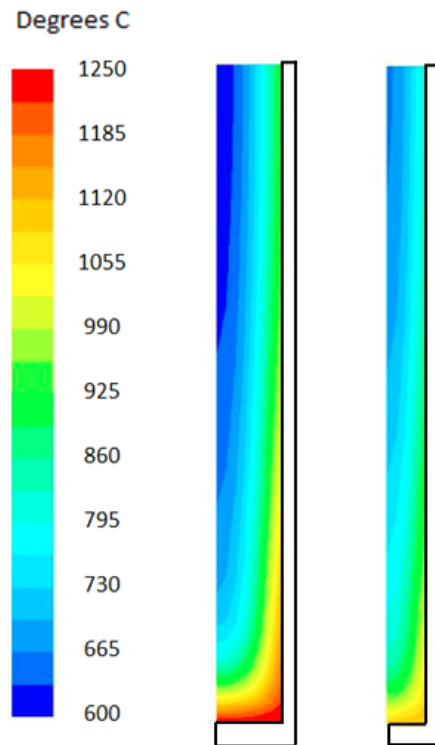


Figure 6.7. Temperature distribution in sand at outlet for configurations C (left) and D (right), with a uniform 600 W m^{-2} radiant flux.

The effect of the depth of the channel can be seen by comparing A to C and B to D. The shorter 50 mm sections (C and D) show higher efficiency, again due to the smaller difference in temperature between the flowing sand and the absorber surface. While reducing the depth increases efficiency, it also implies a higher flow velocity is necessary to maintain the same outlet temperature. By continuing to reduce the section depth, the mass flux limit will eventually be reached, and any further reduction is not possible without entering the free-fall flow regime. An optimal design may be one where the section is just deep enough so the sand flows exactly at the mass flux limit. If it were any deeper, it would be less efficient, and if it were less deep, the flow would violate the mass flux limit. By increasing the velocity, k_{eff} will also increase, which would also lead to higher efficiency.

The most important finding is that thermal efficiency is between 52.7 and 68.9%. For comparison, the efficiency of other receivers is estimated at 50-90% for various Direct Falling Particle Receivers and 75% for Centrifugal Receivers [5]. For all cases modeled, the maximum absorber temperature was found to stay below the

melting temperature of Nickel 201 of 1435 °C. In reality, the maximum temperature should stay a margin below the melting temperature due to weakening of the metal. These two findings are important evidence in answering the original objectives of efficiency and maximum absorber temperature, and they both demonstrate the validity of the DGF receiver type as a viable option, as long as the right geometry is used and the incident heat flux is not excessive for a certain design.

6.6.1 Receiver Modeling with Concentric Radiative Flux

Next, for more realistic conditions, a receiver with fin configuration D was modeled with a concentric radiative flux distribution. Experimental data or modeling with ray tracing software could be used to find the heat flux distribution under certain circumstances, but a concentric approximation is simpler and still quite similar to modeling results presented [9]. Similar to [9], a flux distribution was chosen with a maximum of 600 kW m⁻², diminishing to 200 kW m⁻² at the corners, shown in Figure 6.8.

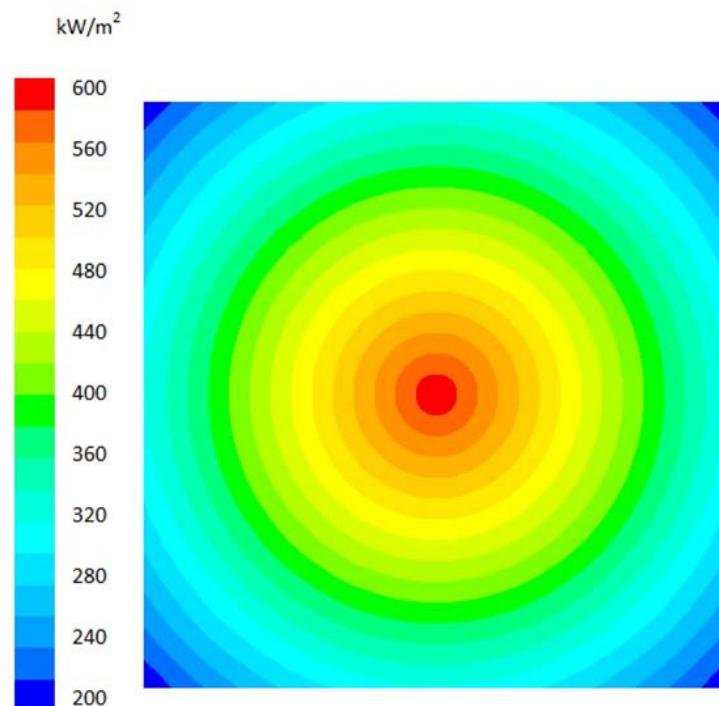


Figure 6.8. Concentric flux distribution on 5 m square receiver.

The concentric radiation boundary condition is applied by the UDF, which calculates the incident radiation at each cell location using Equation (6.6), which was adapted from the equation of the space coordinates of a cone. The incident heat flux at any location, $q_{inc,i}$, is calculated from the x and y coordinates, the peak heat flux, $q_{inc,max}$, the x and y values of the peak, and the radius of the circle with heat flux of 0 W m^{-2} , r.

$$q_{inc,i} = q_{inc,max} - \left[(x - x_{center})^2 + \frac{(y - y_{center})^2}{(r/q_{inc,max})^2} \right]^{1/2} \quad (6.6)$$

Since each fin location has a different heat flux, ideally every fin along the receiver would be modeled. This would be computationally extremely expensive, so the problem was reduced by only modeling a fin every 25 cm along the receiver. This would mean 20 fins to model, but the right and left halves are identical, so only 10 fins must be studied.

The inlet temperature was 500°C , and the flow rate was adjusted iteratively for each fin to achieve an outlet temperature of 800°C . With the highest heat flux in the center of the receiver, the center sections need to run with a higher flow rate to maintain the same 800°C output temperature. An actual receiver could have an outlet valve for each flowing section of sand, and they could be individually adjusted to achieve a desired output temperature. With a real-time temperature reading at the output, valves could be automatically adjusted with a feedback control loop.

6.6.2 Results and Discussion for Concentric Radiant Flux

Table 6.6 shows the results from ten fins which represent the whole receiver. The fin location is in the middle of the representative section. For example, the fin at location 0.125 m represents the part of the receiver from 0 to 0.25 meters. The heat gain and losses were solved for each of the fins and multiplied by the number of fins per section. Configuration D has a width of 5 mm, and the section it represents is 250 mm, so the results for the single fin are multiplied by 50. Results are shown for

only the left half of the receiver, as the right side would be identical. Therefore, the net heat gain by the entire receiver is 6.38 MW. The overall efficiency was calculated by dividing the sum of the net heat gain by the sum of the incident radiation; simply averaging the efficiency numbers would be incorrect as the weight ascribed to each fin is slightly different, given the different heat flux on each section.

Table 6.6. Heat loss and gain for left half of receiver with a concentric radiative flux, divided into ten sections.

Location (m)	Velocity (m/s)	Incident Radiation (kW)	Refl. Loss (kW)	Conv. Loss (kW)	Emiss. Loss (kW)	Net Heat Gain (kW)	Efficiency
0.125	0.086	360	12.6	21.4	96	230	63.8%
0.375	0.0942	390	13.7	21.8	102	253	64.7%
0.625	0.1022	420	14.7	22.2	108	275	65.4%
0.875	0.1102	449	15.7	22.6	114	296	66.0%
1.125	0.1182	476	16.7	23.0	120	317	66.5%
1.375	0.1255	501	17.5	23.3	125	336	66.9%
1.625	0.131	525	18.4	23.6	130	352	67.1%
1.875	0.1365	545	19.1	23.9	135	367	67.3%
2.125	0.1415	561	19.6	24.1	139	379	67.5%
2.375	0.1445	571	20.0	24.2	141	386	67.6%
Total		4798				3189	
Overall Thermal Efficiency							66.5%

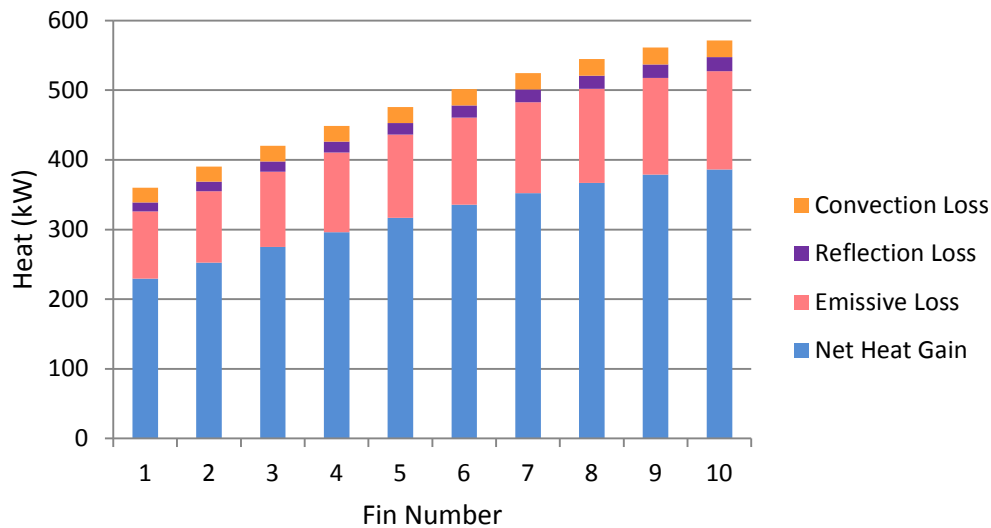


Figure 6.9. Heat gain and losses from various sections of the receiver.

Similar to results with a uniform radiative flux distribution, Table 6.6 shows that a higher incident radiative flux leads to a higher thermal efficiency, but it also

increases the surface temperature (Figure 6.10). This is an important relationship in the design process of a receiver. Assuming the solar field size is fixed, the incident radiative flux on the receiver can be increased by reducing the receiver size. As shown, the receiver efficiency will increase as the heat flux increases, but a limit is imposed by the maximum temperature of the absorber, which also increases with incident radiative heat flux.

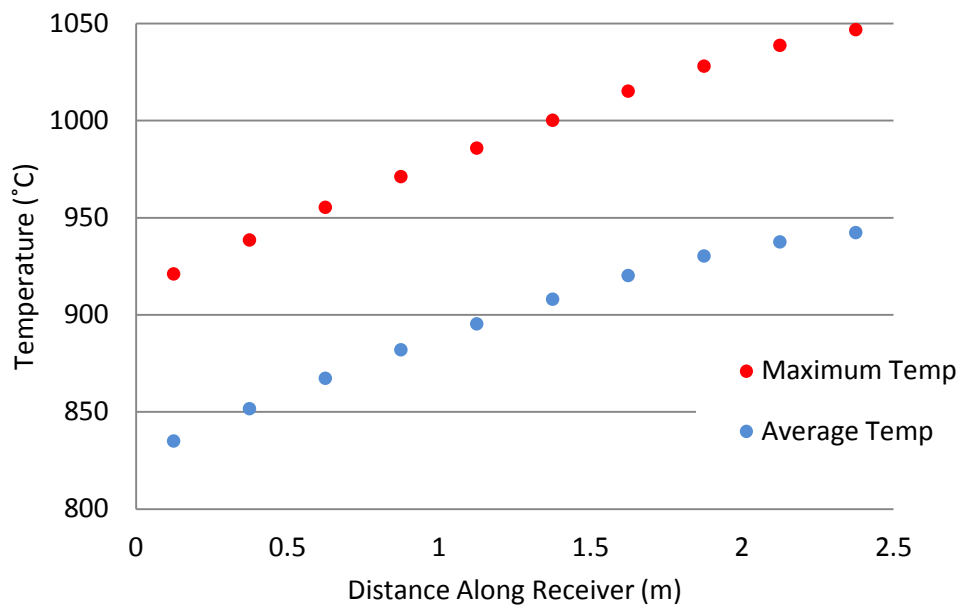


Figure 6.10. Maximum and average temperature of the absorber surface for ten fins modeled.

Figure 6.10 shows that all fins stay well below the 1435°C melting temperature, and as expected the temperatures are highest near the center. The outlet temperature for each section is 800°C, so any temperature in excess of this represents a deviation from a perfect receiver.

CHAPTER 7

CONCLUSIONS

Various designs of solid particle solar receivers are being tested at research institutions around the world. Current designs have significant shortcomings such as difficulty controlling flow, loss of particles, problems in wind, high parasitic electrical loads, fluidization problems with large particles, and low mass flux limits. The design proposed here fixes many of these shortcomings, but the fundamental question is whether particles can effectively transfer enough heat in the dense granular flow regime to A) achieve a high thermal efficiency and B) keep the absorber temperature well below the melting point.

Studying the flow and heat transfer characteristics in tubes provided the fundamental knowledge that would be essential when scaling up to a more complex receiver. It was found that a mass flux limit exists where the flow regime turns from granular to free fall, and the limit increases with the diameter and cross sectional area of the tube. A maximum value was recorded at $379 \text{ kg m}^{-2} \text{ s}^{-1}$ with a 15.25 mm tube, the largest diameter tested. The Fine sand type was found to have a much lower mass flux limit than Medium and Large sand types. Heat transfer coefficients were found to increase with flow rate, and a maximum value of $251 \text{ W m}^{-2} \text{ K}^{-1}$ was found for course sand at a mass flux of $246 \text{ kg m}^{-2} \text{ s}^{-1}$ or velocity 15.3 cm s^{-1} . While understanding these trends are useful, the tubular experiments do not easily translate into a full receiver design, so flow through a heated parallel plate geometry was studied next.

Effective thermal conductivity is a concept used by many researchers, especially in the field of computational fluid dynamics. As an alternative to studying the heat transfer through complex computational methods, experiments were designed to find this value empirically for the conditions of parallel plate flow with heat applied to one side. Plug flow was assumed, which has been used by other researchers and verified experimentally in this study. The experimental setup was modeled in Fluent CFD using a single liquid phase, and various values of thermal conductivity were

tried until modeled and experimental results were a close match. Taking this value as the effective thermal conductivity, CFD modeling was reduced from a complex mixture to a single-phase fluid in plug flow. Results from six experimental runs were averaged to find an effective thermal conductivity value of $0.255 \text{ W m}^{-1} \text{ K}^{-1}$. This was taken as a constant, though it is expected to increase at higher temperatures and flow rates.

With the effective thermal conductivity found, CFD modeling was performed on four different fin geometries under a uniform radiative flux assumption. Results showed thermal efficiencies between 52.7 and 68.9%, and maximum absorber temperatures between 959 and 1298 °C. With certain fin geometries, the receiver can withstand a flux of 600 W m^{-2} without melting, though for others the absorber would be very near its melting point. All fin geometries tested would stay well under the melting temperature with a 300 W m^{-2} radiative flux.

One fin configuration was modeled using a concentric radiative flux assumption with a peak of 600 kW m^{-2} . Calculations show the 5 meter square receiver gathered 6.38 MW and had an efficiency of 66.5%.

With these results, the original two questions have been answered; with the right fin geometry, it is possible to construct a dense granular flow receiver which stays below the melting temperature and achieves a relatively high thermal efficiency. As this is the first study of such a receiver, many parameters will be studied in the future to increase the efficiency. If a comparable thermal efficiency to other solid particle receivers can be achieved while still capturing the practical benefits of the DGF receiver, it may be a viable option for industrial solar power plants in the future.

CHAPTER 8

FUTURE WORK

Thermal efficiency of the receiver is expected to increase with improvements in the receiver design. The methods and experimental setup could be modified to study the effects of various improvements, including the following:

- Optimizing the fin spacing and depth with the current finned design
- Tilting the fins at an angle to enhance heat transfer, as suggested by [18]
- Using alternate receiver materials with higher thermal conductivity, such as ceramics

A large increase in efficiency can be expected by switching from an “external” type receiver to a “cavity” type receiver, where a hood is added to reduce emissive and convective losses. This is especially important at high temperatures due to the high emissive losses and large improvements have been shown by adding such a hood [31].

In addition, k_{eff} of sand was calculated based on the conservative assumption that it was constant with respect to temperature and velocity. Future work should include classifying the relationship of k_{eff} to these parameters, and a higher thermal efficiency will be found.

The maximum mass flux was studied for tube geometries but not for rectangular sections. Future work may include classifying the relationship of mass flux vs. channel size, which would be an important limit to determine when designing a full-scale receiver.

The material chosen was Nickel 201, but alternatively high conductivity ceramics such as silicon carbide may be considered. A design optimized for both heat transfer and cost may be a combination of these high temperature materials. The weight of a finned receiver would be substantial, and any structural constraints were not considered in this study.

Radiative flux to the receiver could be modeled in the future with ray tracing software such as Tonatiuh. With a 3D curve fit, an equation for the heat flux could be directly implemented into the current UDF.

REFERENCES

- [1] Z. Ma, M. Mehos, G. Glatzmaier, and B. B. Sakadjian, “Development of a Concentrating Solar Power System Using Fluidized-bed Technology for Thermal Energy Conversion and Solid Particles for Thermal Energy Storage,” *Energy Procedia*, vol. 69, pp. 1349–1359, May 2015.
- [2] C. Ho, J. Christian, D. Gill, A. Moya, S. Jeter, S. Abdel-Khalik, D. Sadowski, N. Siegel, H. Al-Ansary, L. Amsbeck, B. Gobereit, and R. Buck, “Technology Advancements for Next Generation Falling Particle Receivers,” *Energy Procedia*, vol. 49, pp. 398–407, 2014.
- [3] C. K. Ho, J. M. Christian, J. Yellowhair, N. Siegel, S. Jeter, M. Golob, S. I. Abdel-Khalik, C. Nguyen, and H. Al-Ansary, “On-sun testing of an advanced falling particle receiver system,” *AIP Conf. Proc.*, vol. 1734, 2016.
- [4] J. Hruby, R. Steeper, G. Evans, and C. Crowe, “An Experimental and Numerical Study of Flow and Convective Heat Transfer in a Freely Falling Curtain of Particles,” *J. Fluids Eng.*, vol. 110, no. 2, p. 172, 1988.
- [5] C. K. Ho, “A new generation of solid particle and other high-performance receiver designs for concentrating solar thermal (CST) central tower systems,” *Adv. Conc. Sol. Therm. Res. Technol.*, pp. 107–128, 2017.
- [6] A. B. Morris, Z. Ma, S. Pannala, and C. M. Hrenya, “Simulations of heat transfer to solid particles flowing through an array of heated tubes,” *Sol. Energy*, vol. 130, pp. 101–115, Jun. 2016.
- [7] G. Flamant, D. Gauthier, H. Benoit, J.-L. Sans, B. Boissière, R. Ansart, and M. Hemati, “A New Heat Transfer Fluid for Concentrating Solar Systems: Particle Flow in Tubes,” *Energy Procedia*, vol. 49, pp. 617–626, 2014.
- [8] H. Benoit, I. Pérez López, D. Gauthier, J.-L. Sans, and G. Flamant, “On-sun demonstration of a 750°C heat transfer fluid for concentrating solar systems: Dense particle suspension in tube,” *Sol. Energy*, vol. 118, pp. 622–633, Aug. 2015.
- [9] A. Gallo, J. Spelling, M. Romero, and J. González-Aguilar, “Preliminary Design and Performance Analysis of a Multi-megawatt Scale Dense Particle Suspension

- Receiver,” *Energy Procedia*, vol. 69, pp. 388–397, May 2015.
- [10] W. Wu, L. Amsbeck, R. Buck, R. Uhlig, and R. Ritz-Paal, “Proof of concept test of a centrifugal particle receiver,” *Energy Procedia*, vol. 49, pp. 560–568, 2013.
- [11] W. Wu, D. Trebing, L. Amsbeck, R. Buck, and R. Pitz-Paal, “Prototype Testing of a Centrifugal Particle Receiver for High-Temperature Concentrating Solar Applications,” *J. Sol. Energy Eng.*, vol. 137, no. 4, pp. 041011–041011, 2015.
- [12] M. F. Watkins, N. Carolina, and R. D. Gould, “DENSE GRANULAR FLOWS AS A NEW HEAT TRANSFER FLUID FOR CONCENTRATED SOLAR POWER,” pp. 1–7, 2016.
- [13] Y. N. Chilamkurti and R. D. Gould, “Discrete element studies of gravity-driven dense granular flows in vertical cylindrical tubes,” *Power Energy Conf.*, pp. 1–9, 2016.
- [14] GDR Midi, “On dense granular flows,” *Eur. Phys. J. E*, vol. 14, no. 4, pp. 314–365, 2004.
- [15] P. W. Cleary and M. L. Sawley, “DEM modelling of industrial granular flows: 3D case studies and the effect of particle shape on hopper discharge,” *Appl. Math. Model.*, vol. 26, no. 2, pp. 89–111, 2002.
- [16] G. I. Tardos, “A fluid mechanistic approach to slow, frictional flow of powders,” *Powder Technol.*, vol. 92, no. 1, pp. 61–74, 1997.
- [17] F. P. Incropera, D. P. DeWitt, T. L. Bergman, and A. S. Lavine, *Fundamentals of Heat and Mass Transfer*, vol. 6th. John Wiley & Sons, 2007.
- [18] V. V. R. Natarajan and M. L. Hunt, “Heat Transfer in Vertical Granular Flows,” *Exp. Heat Transf.*, vol. 10, no. 2, pp. 89–107, 1997.
- [19] M. L. Hunt, “Discrete element simulations for granular material flows: effective thermal conductivity and self-diffusivity,” *Int. J. Heat Mass Transf.*, vol. 40, no. 13, pp. 3059–3068, 1997.
- [20] William Noel Sullivan, “Heat Transfer to Flowing Granular Media.” 1973.
- [21] A. C. Iniesta, M. Diago, T. Delclos, Q. Falcoz, T. Shamim, and N. Calvet, “Gravity-fed Combined Solar Receiver/Storage System Using Sand Particles as Heat

- Collector, Heat Transfer and Thermal Energy Storage Media,” *Energy Procedia*, vol. 69, pp. 802–811, May 2015.
- [22] F. Cardarelli, *Materials Handbook (2e)*. 2008.
- [23] C. Mankoc, A. Janda, R. Arévalo, J. M. Pastor, I. Zuriguel, A. Garcimartín, and D. Maza, “The flow rate of granular materials through an orifice,” *Granul. Matter*, vol. 9, no. 6, pp. 407–414, 2007.
- [24] O. E. Dwyer, “On the transfer of heat to fluids flowing in annuli and parallel plates,” *Nucl. Sci. Eng.*, vol. 17, pp. 336–344, 1963.
- [25] V. V. R. Natarajan and M. L. Hunt, “Heat Transfer in Vertical Granular Flows,” *Exp. Heat Transf.*, vol. 10, no. 2, pp. 89–107, 1997.
- [26] J. Marti, A. Haselbacher, and A. Steinfeld, “A numerical investigation of gas-particle suspensions as heat transfer media for high-temperature concentrated solar power,” *Int. J. Heat Mass Transf.*, vol. 90, pp. 1056–1070, 2015.
- [27] T. Baumann and S. Zunft, “Properties of granular materials as heat transfer and storage medium in CSP application,” *Sol. Energy Mater. Sol. Cells*, vol. 143, pp. 38–47, 2015.
- [28] Special Metals, “Product Handbook of Product Handbook of High- Performance Nickel Alloys.”
- [29] A. Ambrosini, M. Gray, and C. Ho, “High-Temperature Solar Selective Coating Development for Power Tower Receivers,” *Proj. Present.*, 2015.
- [30] D. L. Siebers and J. S. Kraabel, “Estimating convective energy losses from solar central receivers,” p. 69, 1984.
- [31] J. Kim, J. S. Kim, and W. Stein, “Simplified heat loss model for central tower solar receiver,” *Sol. Energy*, vol. 116, pp. 314–322, 2015.

APPENDIX A

UDF FOR MODELING HEAT TRANSFER TO ABSORBER SURFACE

```

/*****
UDF for specifying wall flux
*****/

#include "udf.h"

/* Flux is the name of the quantity we want to solve for, t is thread (zone)
/* pointer, and i is the cell pointer. Pointers are passed automatically from Fluent.*/

DEFINE_PROFILE(flux,t,i)
{
    cell_t c;
    face_t f;
    real x[ND_ND]; /*Make array for centroid coordinates*/
    real A[ND_ND]; /*Make array for area*/
    real h = 21; /*Convection coefficient*/
    real T_amb = 293.15; /*Ambient temperature*/
    real sigma = 5.67e-8; /*Stephan-Boltzman constant */
    real emiss = .87; /*Emissivity of absorber surface*/
    real alpha = 0.965;
    real q_inc; /*Incident radiative flux */
    real q_refl;
    real q_conv; /*Convection flux */
    real q_rad; /*Radiative loss */
    real q_net; /*Net heat flux into element of absorber surface */
    real X;
    real Y;
    real Z;

    real area;
    real T_surf; /*Absorber surface temperature */

    /* Change the incident flux with these parameters*/
    real q_inc_max = 600000;
    real z_ctr = 2.5; /* z coordinate of the center*/
    real r = 1.5*2.5*1.4142; /*Radius of cone of radiant flux*/
    real x_fin = 0; /*x-coordinate of the fin to study (actually changes the x-pos of the cone to 2.5-x_fin).*/

    /* Open a text file for writing (w)*/
    FILE * fid;
    fid = fopen("flux", "w");

    /* Loop over all faces (f) within the current thread (t), passed to program based on which boundary it's called
    from. */
    begin_f_loop(f, t)
    {
        /* Find the x, y, and z values of the centroid of the face. Centroid coordinates stored in the 3-value array, [x] */
        F_CENTROID(x,f,t);

        X = x[0];
        Y = x[1];
        Z = x[2];
    }
}

```

```

/* find the surface temperature of the current face, and call it T_surf*/
T_surf = F_T(f,t);

/*Use the equation of a cone to find the incident q at each element's location*/
q_inc = q_inc_max - pow(((pow((X-(2.5-x_fin)),2) + pow((Z-z_ctr),2))/(pow((r/q_inc_max),2)) ),.5);

/* To use a uniform heat flux, uncomment the following line, and comment out the equation above*/
/*q_inc = 300000;*/

/* Cone equation sets heat flux of some areas to a negative value, so set these to 0 */
if (q_inc < 0)
{
q_inc = 0;
}

/* Account for convective and radiative losses*/
q_refl = (1-.965)*(q_inc);
q_conv = h*(T_surf-T_amb);
q_rad = sigma*emiss*(pow(T_surf,4) - pow(T_amb,4));
q_net = q_inc - q_refl - q_conv - q_rad;

/* set the heat flux into element's face (f) to the calculated heat flux */
F_PROFILE(f,t,i) = q_net;

/* find the area of that face*/
F_AREA(A,f,t);

area = A[1];

/*print the face number, area, q_inc, q_conv, q_rad, and q_net into a text file*/
fprintf(fid, "%d %1.11f %4.0f %4.0f %4.0f %4.0f %4.0f %4.1fn", f, area, q_inc, q_refl, q_conv, q_rad, q_net,
T_surf);

}
end_f_loop(f, t)

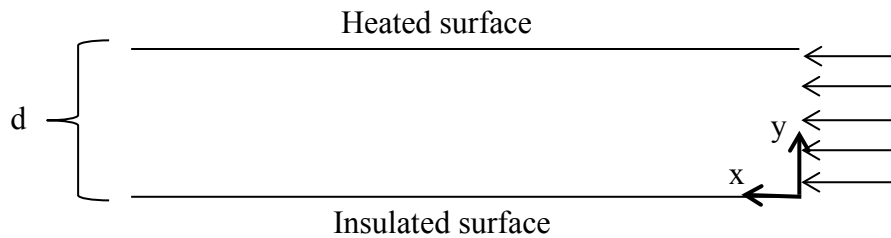
fclose(fid);

} /* end DEFINE_PROFILE */

```

APPENDIX B

NUSSELT NUMBER DERIVATION FOR PLUG FLOW THROUGH INFINITE PARALLEL PLATES



Assuming laminar flow and negligible conduction in the x -direction, the governing heat transfer equation is given in (1), where u is the velocity and α is the thermal diffusivity.

$$u \frac{\partial T}{\partial x} = \alpha \frac{\partial^2 T}{\partial y^2} \quad (1)$$

With a constant heat flux boundary condition, in the fully developed region, all temperatures rise linearly with distance from the inlet at the same rate the mean (bulk) temperature increases:

$$\frac{\partial T}{\partial x} = \frac{dT_m}{dx} \quad (2)$$

Substituting in dT_m/dx and integrating twice:

$$T = \frac{u}{\alpha} \frac{dT_m}{dx} \frac{y^2}{2} + c_1 y + c_2 \quad (3)$$

Boundary conditions are:

$$\frac{\partial T}{\partial y} = 0 \text{ at } y = 0 \quad (4)$$

and

$$T = T_s \text{ at } y = d \quad (5)$$

Where T_s is the surface temperature, which is a function of x .

Solving for c_1 and c_2 with boundary conditions,

$$T = \frac{u}{2\alpha} \frac{dT_m}{dx} (y^2 - d^2) + T_s \quad (6)$$

T_m can be found with the average value theorem:

$$T_m = \frac{\int_0^d T u dy}{d} = \frac{1}{d} \left[\frac{U}{2\alpha} \frac{dT_m}{dx} \left(\frac{y^3}{3} - d^2 y \right) + T_s y \right]_0^d \quad (7)$$

$$T_m = T_s - \frac{U}{3\alpha} \frac{dT_m}{dx} \quad (8)$$

Now, to find an expression for dT_m/dx ,

$$\frac{dT_m}{dx} = \frac{q'' w}{\dot{m} C_p} \quad (9)$$

Where w is the arbitrary depth of the section in the z -direction and mass flow rate is defined as:

$$\dot{m} = \rho u (d * w) \quad (10)$$

dT_m/dx can be expressed as:

$$\frac{dT_m}{dx} = \frac{q''}{\rho U d C_p} \quad (11)$$

Substituting (11) into (8),

$$T_m - T_s = -\frac{dq''}{3k} \quad (12)$$

With Newton's law of cooling,

$$q'' = h(T_s - T_m) \quad (13)$$

Substituting (12) into (13),

$$\frac{hd}{k} = 3 \quad (14)$$

With hydraulic diameter definition, A being the flow area and P being the wetted perimeter:

$$D_h = \frac{4A}{P} \quad (15)$$

$$D_h = \frac{4dw}{2w + 2d} \quad (16)$$

In the limit where w becomes very large,

$$D_h = 2d \quad (17)$$

Substituting D_h into (14), the Nusselt number is found:

$$\frac{hD_h}{k} = 6 \quad (18)$$